Energy 351 (2026) 140598

Contents lists available at ScienceDirect

Energy

journal homepage: www.elsevier.com/locate/energy

Numerical analysis of radiative cooling behavior: Advancing the study of materials' potential for urban overheating mitigation

Chiara Chiatti [a,b], Claudia Fabiani [a,c], Anna Laura Pisello [a,c],*

[a] EAPLAB at CIRIAF Interuniversity Research Centre on Pollution and Environment "M. Felli", University of Perugia, Via G. Duranti 63, Perugia, 06125, Italy
[b] Department of International Human and Social Sciences, University for Foreigners of Perugia, Piazza B. Fortebraccio 4, Perugia, 06123, Italy
[c] Department of Engineering, University of Perugia, Via G. Duranti 97, Perugia, 06125, Italy

ARTICLE INFO

Keywords:
Passive cooling
Radiative cooling
Urban overheating
Cool materials
COMSOL multiphysics

ABSTRACT

The rapid increase in population, energy-saving demands, the need for indoor–outdoor thermal comfort, combined with rising global temperatures, highlight the urgency for efficient cooling strategies in the built environment. This study investigates aluminum- ("A") and Vikuiti- ("V") based materials for passive radiative cooling (RC), designed with tailored thermo-optical properties compared to a pure aluminum sample ("ref"). After the experimental characterization of the samples, a Finite Element Method (FEM) model is developed and validated to simulate the RC performance under typical mid-latitude summer and winter conditions. This approach enables accurate prediction of seasonal behavior, reducing experimental effort and resource consumption. Results confirm the model's capability to reproduce the RC phenomenon, particularly the radiative exchange within key spectral wavebands. Among the tested materials, the "V" sample achieves a sub-ambient cooling of −9.7 °C under summer conditions with minimal convective influence, emphasizing the critical role of spectral selectivity in material design for real-world applications. Furthermore, a parametric analysis investigates RC potential under hypothetical spectral configurations and varying atmospheric transmittance, extending the model's applicability and offering insights for optimizing passive cooling solutions.

1. Introduction

Human activities have significantly contributed to urban climate change, leading to rising global temperatures and more frequent extreme weather events [1]. This trend is particularly pronounced in cities, where the Urban Heat Island (UHI) effect causes urban areas to exhibit higher air and surface temperature than rural surroundings [2], with projections indicating up to 3 °C increase in urban temperatures by 2100 [3]. The environmental ramifications – including elevated energy demand for cooling, increased air pollution, and greater greenhouse gas emissions – fuel a feedback loop that exacerbates urban warming. UHI is driven by a variety of anthropogenic factors: population growth, high-density impermeable surfaces, and altered surface energy balances [4,5]. As buildings account for over one-third of global energy use and emissions [6], comprehensive strategies are urgently needed to mitigate the environmental, economic and thermal negative impacts of UHI [7,8].

In response, passive cooling solutions have been deeply explored during the last decades, with radiative cooling (RC) emerging as one of the most promising approaches to reduce building surface and indoor temperatures [9,10]. The RC mechanism consists of dissipating heat by radiatively exchange with outer space, exploiting specific wavebands, called atmospheric windows (AWs) [11]. Effective RC occurs when a surface's thermal emission to space exceeds the heat absorbed from solar and atmospheric sources, especially via the 8–13 μm AW: here, the atmosphere offers minimal obstruction, allowing thermal radiation to escape directly into space (at ∼3 K). Nonetheless, urban environments present notable challenges: real-world RC materials interact with multiple factors influencing their thermal behavior, including conductive and convective heat exchanges with the surrounding, incident solar radiation, and atmospheric back-radiation. All these aspects, especially the absorption of solar radiation, hinder the RC efficiency, making daytime cooling more challenging than nighttime [12–14]. Consequently, material innovations with high solar reflectance and high thermal emittance have been prioritized as essential for next-generation RC systems [15–18].

The first generation of "cool materials" included white reflective paints [19,20], followed by colored coatings with near infrared (NIR) reflectance to better suit aesthetic demands of urban infrastructures [21,22]. Despite the improvements, these materials often showed limited RC efficiency. RC systems are broadly classified into selective (SRC)

---

* Corresponding author at: Department of Engineering, University of Perugia, Via G. Duranti 97, Perugia, 06125, Italy.
E-mail addresses: chiara.chiatti@unistrapg.it (C. Chiatti), claudia.fabiani@unipg.it (C. Fabiani), anna.pisello@unipg.it (A.L. Pisello).

https://doi.org/10.1016/j.energy.2026.140598
Received 17 September 2025; Received in revised form 25 January 2026; Accepted 26 February 2026

Nomenclature

AW	Atmospheric window
BRC	Broadband radiative cooling
EPS	Extruded polystyrene
FIR	Far infrared spectrum (>20 μm)
MAE	Mean absolute error
MIR	Mid-infrared spectrum (2.5–20 μm)
NIR	Near infrared spectrum (0.78–2.5 μm)
PMSQ	Polymethilsilsequioxane
RC	Radiative cooling
RMSE	Root mean square error
SRC	Selective radiative cooling
SRI	Solar Reflectance Index
UHI	Urban Heat Island
UV	Ultraviolet spectrum (<0.38 μm)
VIS	Visible spectrum (0.38–0.78 μm)
κ	Thermal conductivity [W/mK]
λ	Wavelength [μm]
ρ	Reflectance [%]
σ	Stefan-Boltzmann constant (5.67×10^{-8} W/m^{2}K^4)
τ	Transmittance [%]
ε	Emittance [%]
$\mathbf{q}$	Heat flux vector [W/m^3]
$\mathbf{u}$	Velocity vector [m/s]
c_p	Specific heat [J/kgK]
d	Density [kg/m^3]
e_b	Blackbody emissive power [W/m^2]
F	View factor [–]
FEP	Form factor emissive power correction [–]
h	Heat transfer coefficient [W/m^{2}K]
I	Incident irradiation [W/m^2]
n	Refractive index of a medium [–]
q	Heat flux [W/m^2]
T	Temperature [°C]
t	Time [s]
exp	Experimental
sim	Simulated
air	With reference to the ambient air
amb	Ambient
atm	With reference to the atmosphere
c	With reference to convective exchange
ext	External
$inAW$	Within the AW (8–13 μm)
k	With reference to conductive exchange
m	Mutual, between surfaces
max	Maximum value
$outAW$	Outside the AW (2.5–8 μm and >13 μm)
r	With reference to radiative exchange
sky	With reference to the sky
sol	Solar
$space$	With reference to the outer space
sup	Superficial

and broadband (BRC) types: SRCs target emission within the 8–13 μm AW, whereas BRCs emit across the broader infrared spectrum [23,24]. For RC large-scale adoption, durability, costs, and scalability are widely recognized as critical factors. Though high-performance prototypes exist, many are expensive and hard to scale [25]. Coatings are currently the most promising approach due to their ease of application, cost-effectiveness and versatility [26,27]. However, durability remains a challenge: UV exposure, soiling and aging often leads to material degradation, resulting in reduced cooling efficiency over time and in a worsening of optical and thermal properties [28].

Despite rapid advances, key gaps and limitations impede broader adoption of RC materials in real-world settings [29]. Most studies emphasize the immediate cooling performance of RC prototypes, often neglecting critical aspects such as long-term durability and resistance to environmental degradation [30,31]. Furthermore, there is a marked gap between lab-scale results and real-world performance, with outdoor testing frequently revealing inconsistencies [32]. For example, the same material developed by Raman et al. [33] failed to achieve sub-ambient temperatures when tested in Hong Kong's climate, demonstrating sub-cooling only at nighttime [34]. Similarly, the highly reflective and thermally emissive coating by Bao et al. [35] only achieved above-ambient temperature in Shanghai, at 30 °C and 70% of relative humidity. These discrepancies highlight the sensitivity of RC performance to environmental factors, particularly humidity and cloud cover, which reduce the transparency of the 8–13 μm AW by increasing thermal radiation absorption by water vapor [36].

Due to the variability of outdoor conditions, indoor replicable testing is considered for evaluating RC materials. However, the lack of standardized testing and reporting practices so far leads to inconsistent results and hinders the comparability of different solutions, thus slowing technological advancement and market uptake [37]. Currently, no experimental metric allows for fair performance comparisons. For instance, the widely used Solar Reflectance Index (SRI) [38] combines a material's solar reflectance and thermal emittance considering both as averaged values, rather than accounting for their spectral distribution. This approach is completely unfavorable for evaluating RC prototypes, since their effectiveness, compared to traditional cooling solutions, depends on reflectance and emittance profiles across the solar and infrared spectra, with particular emphasis on the 8–13 μm AW [39,40]. Moreover, recreating realistic environmental conditions in the controlled indoors poses significant challenges. While climatic chambers can control temperature, humidity, and irradiation to simulate various climates [41,42], they prevent the tested materials from being exposed to real atmosphere, thereby excluding any potential real radiative exchange with outer space [40]. As a result, the true sub-ambient cooling potential of advanced RC materials may remain undetected, making them appear no more effective than conventional cool materials in such setups.

In light of these challenges, advanced modeling techniques offer considerable promise to bridge the gap between material innovation and practical application. Notably, the Finite Element Method (FEM) provides a consolidated platform for simulating heat transfer phenomena, offering nuanced insights into temperature distributions and energy fluxes under complex boundary conditions [43]. Additionally, FEM tools facilitate virtual prototyping, reducing reliance on costly experimental campaigns and accelerating therefore the development of high-performance materials by simulating their behavior under realistic environmental conditions [44,45]. This approach streamlines the transition from laboratory-scale experiments to full-scale applications, offering the flexibility to incorporate specific urban factors that may influence the overall performance of the investigated material.

Against this background, the contribution of the present work is not the generic use of FEM for thermal analysis, but the development of a validated, spectrally resolved framework that tightly couples comprehensive optical characterization with transient heat-transfer modeling of RC materials. The model quantitatively disaggregates the radiative fluxes into distinct spectral bands (0.25–2.5 μm - solar, 8–13 μm - AW, 2.5–8 μm and 13–20 μm - out-of-AW region), thereby providing deeper physical insight into how tailored materials' spectral properties translate into cooling performance under realistic outdoor conditions.

The study moves from the modeling of aluminum- and Vikuiti-based materials, recently proposed by Carlosena et al. [46] as scalable and cost-effective RC solutions, to further expand the analyses toward hypothetical selective and broadband prototype to investigate the impact of: (i) varying materials' spectral properties and (ii) multiple atmospheric conditions. Indeed, a further novel aspect of the present work is the indirect inclusion of different climatic conditions by prescribing climate-specific atmospheric transmittance profiles, derived from established atmospheric radiative models, directly within the models' inputs. This strategy enables the impact of air humidity and longwave transparency on the RC effectiveness to be assessed without resorting to computationally intensive radiative-transfer solvers, thus offering a computationally efficient yet physically consistent bridge between material-scale experiments and climate-sensitive performance predictions.

FEM-based approaches have already been employed to study RC, particularly for the electromagnetic design of metasurfaces and multilayer structures, as well as for evaluating the thermal behavior of specific coatings under idealized conditions [44,47,48]. However, these studies typically focus either on the optical response or on band-averaged thermal performance, without tightly coupling comprehensive spectral characterization with transient, component-scale heat-transfer simulations under realistic boundary conditions [43]. Moreover, existing models rarely provide a quantitative division of radiative fluxes into different wavebands, and only occasionally consider climate variability through simplified or case-specific assumptions [49]. In contrast, the present work advances the state-of-the-art by combining experimentally measured spectral properties with a validated, time-resolved FEM framework that resolves radiative exchanges across distinct spectral bands and incorporates climate-dependent atmospheric transmittance profiles. This integrated and spectrally resolved approach offers a more physically transparent and practically oriented bridge between laboratory characterization and real-world RC performance assessment than previously demonstrated.

2. Materials and in-lab characterization

2.1. Case-study materials

Fig. 1 shows the three considered prototypes (5 cm × 5 cm each) and their main geometric and structural features. A pure aluminum sample ("ref") was taken as reference material and compared to two RC samples, whose structure comprised two different substrates: a reflective aluminum-based substrate (sample "A") and a Vikuiti-based substrate (sample "V"). Both were coupled with an emissive layer consisting of polymethilsilsequioxane (PMSQ) spray coating with SiO_2 particles embedded at a 5% weight. Such combination came from the silica's transparency in the visible (VIS) range, up to 2.5 μm, and its high absorbance in the near/mid-infrared spectrum [50]. Conversely, aluminum has a high reflectance from the near UV to mid-infrared (MIR) [51]. The 3M Vikuiti Enhanced Solar Reflector, instead, was explored as an alternative substrate with an even higher reflectance than the aluminum (∼98% across the solar spectrum) [32]. In a recent study [40], the same RC samples were investigated highlighting the critical need for a comprehensive characterization protocol that considers the full spectral distribution of key thermo-optical properties.

2.2. Thermo-optical characterization procedure

Relying solely on a single value for solar reflectance or thermal emittance – as required by many standards – could lead to the inaccurate assessment of a material RC potential, particularly when compared to conventional passive cooling solutions [39]. For this reason, the samples investigated in this study were tested in terms of reflectance, transmittance and emittance across the UV–VIS-MIR regions of the electromagnetic spectrum. These measurements served also as benchmarks to verify that the materials exhibited the required attributes to be qualified as RCs — namely, high solar reflectance in the shortwave range and a high thermal emittance in the AW (8–13 μm). Reflectance (ρ) and transmittance (τ) in the 0.25–2.5 μm range were measured using a PerkinElmer Lambda 1050+ UV/VIS/NIR spectrophotometer equipped with a 15-cm-diameter integrating sphere. Calibration was performed prior to each measurement session using a certified Spectralon reference standard, and baseline corrections followed the manufacturer's protocol. Three measurements for each sample were carried out and the average profiles were reported in Fig. 2a. For the 2.5–20 μm range, reflectance and transmittance were obtained using a PerkinElmer Spectrum 3 NIR/MIR/FIR spectrometer equipped with a 7.6-cm-diameter PIKE gold-coated integrating sphere. Background spectra were collected before the measurement session, and a gold reference plate was used for calibration. Measurement repeatability was assessed through multiple scans. The emittance (ε, Fig. 2b) was then derived according to Kirchhoff's law: $\varepsilon(\lambda) = 1 - \rho(\lambda) - \tau(\lambda)$.

Both "A" and "ref" samples showed a good reflectivity throughout the solar spectrum, reflecting 60%–70% of the incident UV and VIS radiation, and up to 90% in the near-infrared (NIR) region. In contrast, the Vikuiti-based prototype ("V" sample) showed a remarkable reflectance (∼100%) within the VIS waveband up to 1.25 μm, before transitioning to high transparency (∼86%) in the NIR region. Focusing on the MIR spectrum, despite "A" sample was designed to be a SRC, its emittance reached a peak of only 25% within the AW, around 9.5 μm, while maintaining a low profile (∼10%) across most of the MIR spectrum. "V" sample, instead, showed again promising performance, maintaining a relatively high and consistent emittance (>80%) in the range between 5.5 μm and 14 μm: for this reason, it could be classified as a good BRC. All these spectral responses were implemented within the FEM model of the materials.

2.3. Climatic chamber thermal monitoring

The monitoring of the thermal performance of the case-study materials was carried out using an advanced ATT UD150C climatic chamber equipped with a BF SUN 1200 W solar simulator (Fig. 3a). Samples were individually placed over an extruded polystyrene (EPS) support (30 cm × 30 cm × 21 cm) to prevent downward heat conduction, and their surface temperature was continuously recorded by three sensors (thermocouples, type T) attached to the downward face of each sample in order to avoid direct heating from the solar simulator (Fig. 3b). Data were collected at a time-step of 10 s, and the average of the three sensors was then considered. The experimental system (sample + EPS support) was placed inside the internal compartment of the climatic chamber and exposed for three hours to static and controlled boundary conditions. In particular, ambient temperature and solar irradiation on the samples' surface were respectively set to 30 °C and 880 W/m^2, mirroring the average values of a typical summer day in temperate climates. Surface temperature profiles recorded during this methodological step were used to validate the FEM model of the investigated materials, while replicating the conditions imposed inside the climatic chamber.

3. Development of the numerical model

3.1. Geometric model and materials' properties

The same experimental setup, i.e., the sample placed over the EPS support, was reproduced using COMSOL Multiphysics. A dedicated FEM model was developed for each case-study material, keeping the same dimensions of the physical system. Specifically, the EPS support measured 30 cm × 30 cm × 21 cm (length × width × height), while the dimensions of the samples were as follows: 5 cm × 5 cm × 0.05 cm for the "ref" sample, 5 cm × 5 cm × 0.074 cm for sample "A", and 5 cm × 5 cm × 0.009 cm for sample "V". To accurately reproduce the

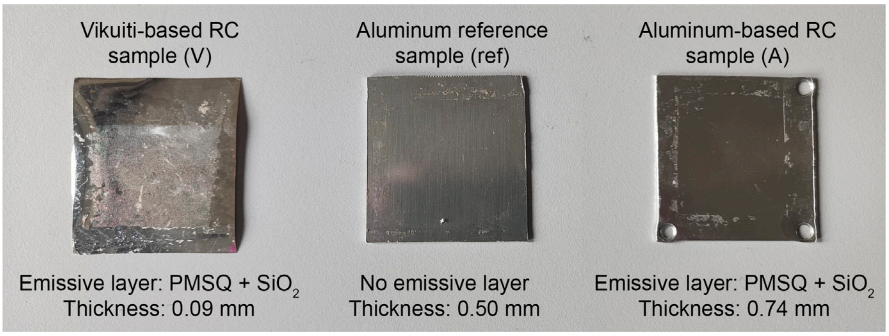

Fig. 1. Geometry and composition features of the case-study materials: Vikuiti-based (“V”), aluminum-based (“A”), and reference (“ref”) sample.

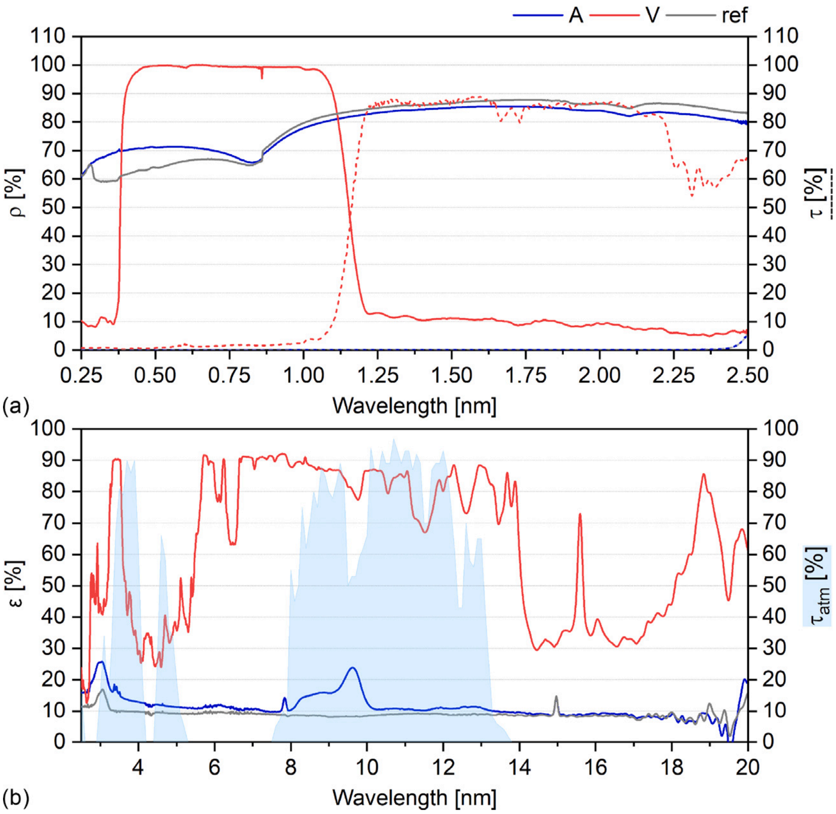

Fig. 2. (a) Reflectance (ρ, continuous line) and transmittance (τ, dotted line) profiles of the case-study materials in the range between 0.25–2.5 μm. (c) Emittance (ε) profiles of the investigated samples compared to the transmittance of the atmosphere (τ_{atm}, light blue colored) in the range between 2.5–20 μm.

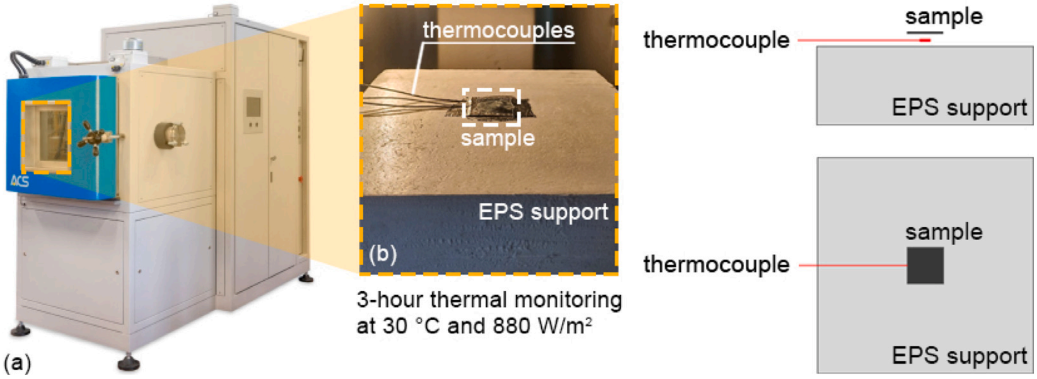

Fig. 3. (a) ATT UD150C SR climatic chamber equipped with a solar simulator and (b) experimental setup in the internal compartment of the chamber for the thermal monitoring of the investigated samples.

Table 1
Input parameters for the FEM models.

Parameter	Unit	ref	A	V	EPS base
Density (d)	kg/m^3	2.53×10^3	2.13×10^3	1.75×10^3	1.15×10
Specific heat (c_p)	J/kgK	8.97×10^2	1.56×10^3	1.56×10^3	1.45×10^3
Thermal cond. (κ)	W/mK	2.22×10^2	2.22×10^2	1.57×10^{-1}	5.00×10^{-2}

radiative behavior of the materials across the UV to MIR spectral range, the measured emittance profiles (obtained as per Section 2.2) were implemented as input functions in the models. The other key physical properties of the involved materials are summarized in Table 1.

3.2. Governing equations

COMSOL Multiphysics is a general-purpose multi-field software that allows for the combination of available built-in and/or user-defined interfaces to investigate various multiphysics problems. The evaluation of the radiative cooling potential of the case-study materials was carried out exploiting the "Heat transfer" module, and in particular the interaction between the "Heat transfer in solids" and the "Surface-to-surface radiation" interfaces. The first solves the energy conservation of thermal energy, accounting for conduction and convective heat transfer, while the second models heat radiation moving from the equation of the total radiosity of a surface, i.e., the radiant flux leaving the surface itself. In transient conditions, the main governing equations for the two interfaces are:

1. $dc_p\frac{\partial T}{\partial t} + dc_p\mathbf{u}\cdot\nabla T + \nabla\cdot\mathbf{q}_k = Q$
   where:

   - $dc_p\frac{\partial T}{\partial t}$ is the transient term accounting for the time-dependent storage of thermal energy in the material;
   - $dc_p\mathbf{u}\cdot\nabla T$ is the convective term representing the heat transport due to fluid motion ($\mathbf{u}$ is the velocity vector of the fluid);
   - $\nabla\cdot\mathbf{q}_k$ is the conductive term, representing the spatial variation of heat flux, typically governed by Fourier's law ($\mathbf{q} = -\kappa\nabla T_k$).

2. $J = \varepsilon\cdot e_b(T)\cdot FEP(T) + \rho\cdot I$ expresses the radiosity of a surface, i.e. the total radiant flux leaving the surface. Here:

   - ε is the surface emissivity, while ρ is the surface reflectivity ($\rho = 1-\varepsilon$, for opaque materials);
   - $e_b(T) = n^2\sigma T^4$ is the ideal blackbody emissive power according to Stefan–Boltzmann law, where σ is the Stefan–Boltzmann constant, T the absolute temperature in Kelvin, and n is the refractive index of the medium (for vacuum or air, $n = 1$);
   - $FEP(T) = \frac{15}{\pi^4}\int_{c_2/(\lambda_1 T)}^{c2/(\lambda_2 T)}\frac{x^3}{1-e^x}dx$ is the fractional emissive power, a dimensionless function representing the fraction of the blackbody radiation emitted between two wavelengths (λ_1 and λ_2), at temperature T. $c_2 = \frac{hc}{k}$ is the second radiation constant;
   - $I = I_m + I_{amb} + I_{ext}$ where I_m is the mutual irradiation from other surfaces, I_{amb} is the ambient background radiation and I_{ext} is an external source of irradiation, like the Sun.
   - $I_{amb} = F_{amb}\cdot\varepsilon_{amb}\cdot e_b(T_{amb})\cdot FEP(T_{amb})$ quantifies the ambient radiation coming from the surroundings and treated as a diffuse black or gray environment at temperature T_{amb}. F_{amb} is the ambient view factor, i.e., the fraction of the considered surface's view that "sees" the ambient. The ambient environment is described by means of its emissivity (ε_{amb}) and temperature (T_{amb}).

3.3. Boundary conditions

FEM models accounted for all relevant heat transfer mechanisms involving the sample, the EPS support, and the surrounding environment:

- conduction between the sample and the EPS support;
- convection between the sample and the ambient air;
- radiative heat transfer between the sample and the environment, either the climatic chamber or the outdoor setting.

Adiabatic boundary conditions were applied on the lateral faces of the EPS support, assuming no heat exchange with the surrounding air. Ambient temperature (T_{amb}) was imposed along all external edges of the sample, ensuring consistent thermal interaction with the environment. Convective heat transfer (q_c), instead, was considered on the upward face of the sample using the same T_{amb} as main driver of the flux exchange: $q_c = h_c(T_{sup} - T_{amb})$, being h_c the convective heat transfer coefficient and T_{sup} the surface temperature of the sample. Concerning radiative exchanges (q_r), all the involved materials were defined as diffuse-gray emitters, implementing the experimentally obtained ε spectral profiles in the models, from 0.25 to 20 μm. Finally, an external irradiation source was applied at an infinite distance from the sample, pointing toward its upward face, in order to account for possible solar gains ($T_{ext} = 5780K$).

4. Design of numerical analyses

As previously described, we developed FEM models reproducing the experimental setup consisting of the EPS support with the case-study sample ("ref", "A" or "V") centrally positioned on top. A first validation analysis (Section 4.1) was carried out by simulating the system inside the internal compartment of the climatic chamber, in order to assess whether simulated outputs aligned with experimentally monitored data. Subsequently, the RC potential of the investigated samples was analyzed by simulating the same system under outdoor conditions of exposure, implementing the radiative exchange within the AW (Section 4.2). Fig. 4 provides a schematic overview of the numerical framework adopted in this study, illustrating the FEM model and the two types of transient simulations performed. The specific assumptions, boundary conditions, and physical processes associated with each analysis are described in detail in the following paragraphs.

4.1. Validation of the model

The validation process consisted of the comparison between experimental and simulation results. To this end, the same environmental conditions used during the thermal monitoring inside the climatic chamber were reproduced (Fig. 4a). The modeled system (sample + EPS support) was exposed to an ambient environment with the same emissivity of the chamber's internal surfaces ($\varepsilon_{amb} = 0.4$), while the convective heat transfer coefficient h_c was set to 2.5 W/m^{2}K. An ambient temperature (T_{amb}) of 30 °C and an external solar irradiation (I_{sol}) of 880 W/m^2 were imposed as boundary conditions to properly replicate the controlled cycle described in Section 2.2. A steady-state simulation was first conducted for each sample to initialize the model and establish the initial conditions for the subsequent 3-hour transient simulation, replicating the climatic chamber test (T_{amb} = 30 °C, I_{sol} = 880 W/m^2). The average temperature of the sample's upward surface was considered as output for comparison with experimental data. To assess the accuracy of the FEM models, the agreement between experimental and simulated surface temperature data (T_{sup}) was further quantified by means of the root mean square error (RMSE, Eq. (1)) and the mean absolute error (MAE, Eq. (2)):

$$RMSE = \sqrt{\frac{1}{N}\sum_{i=1}^{N}(T_{sup}^{sim} - T_{sup}^{exp})^2} \tag{1}$$

$$MAE = \frac{1}{N}\sum_{i=1}^{N}|T_{sup}^{sim} - T_{sup}^{exp}| \tag{2}$$

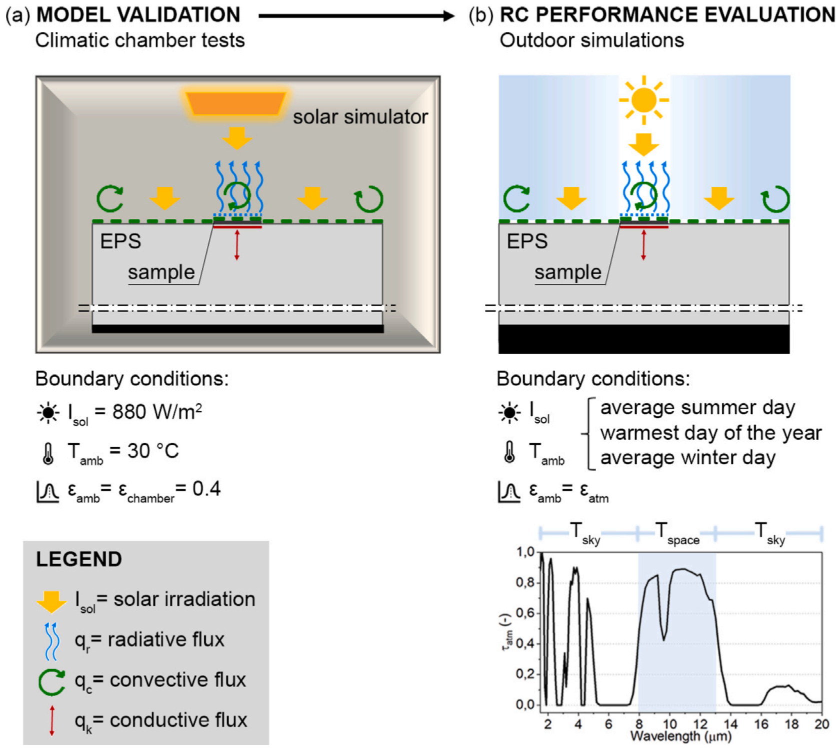

Fig. 4. Schematic representation of the FEM model and the heat transfer mechanisms considered in case of (a) model validation (b) RC performance evaluation.

4.2. RC performance evaluation

The same validated models were employed to evaluate the RC potential of the studied materials under realistic outdoor conditions (Fig. 4b). The average summer and winter days of a temperate climate were selected as boundary environmental conditions, together with the warmest day of the year. Meteorological data were collected by a weather station located on the rooftop of CIRIAF building in Perugia (Italy). The average summer scenario was defined by calculating the hourly mean values of air temperature and global solar irradiation recorded between June 21 and September 22, 2023. Similarly, the average winter scenario comprehended the same type of data from January 1 to March 20 of the same year. Based on 2023 data, the peak temperature day of the year was August 24, when T_{amb} reached 37.6 °C and solar irradiation peaked at 975.6 W/m^2. Figs. 5a-c show ambient temperature (T_{amb}) and solar irradiation (I_{sol}) profiles of the three selected days. For each day, a steady-state simulation was carried out to set up the model and define the initial conditions (T_{amb} = 20 °C and I_{sol} = 0 W/m^2 for the summer case, T_{amb} = 26 °C and I_{sol} = 0 W/m^2 for the warmest day, and T_{amb} = 5 °C and I_{sol} = 0 W/m^2 for the winter case). Subsequently, a 24-hour transient simulation replicating the whole day was performed, focusing on the average surface temperature of the sample, the convective heat transfer with the surrounding, and the radiative exchange in different wavebands as main numerical outputs.

To properly simulate the radiative exchange between the sample and the surrounding environment, assuming the sample facing the sky, the spectral distribution of the atmospheric emittance typical of Perugia's climate was implemented in the FEM model ($\varepsilon_{amb} = \varepsilon_{atm}$). Being the atmosphere highly transparent within the AW (Fig. 5d), the magnitude of the radiative heat exchange was driven by the difference between:

- the temperature of the sample (T_{sup}) and the outer space ($T_{space} \sim 3K$), in the range 8–13 μm: $q_{r,inAW} = \sigma\varepsilon_{atm,inAW}(T_{sup}^4 - T_{space}^4)$;
- the temperature of the sample (T_{sup}) and the sky (T_{sky}), outside the AW: $q_{r,outAW} = \sigma\varepsilon_{atm,outAW}(T_{sup}^4 - T_{sky}^4)$.

These simulations were repeated for three different convective heat transfer coefficients h_c, i.e., 5, 12 and 30 W/m^{2}K, in order to evaluate he RC performance of the samples under low-, medium- and high-wind scenarios, respectively [52].

4.3. Modeling assumptions and limitations

The FEM models operated on the following thermo-physical assumptions:

- *Materials' properties*
  - The emissivity of the investigated materials was simulated using their spectral profiles, spanning the 0.25–20 μm range with a wavelength resolution of 0.05 μm. This approach enabled a more accurate assessment of the impact of spectral emittance – particularly within the atmospheric window (AW) – on the overall RC performance, as compared to non-RC materials.
  - The thermal conductivity of both "ref" and "A" samples was set equal to that of aluminum alloy 1050, corresponding to the substrate material of sample "A". The contribution of the SiO$_2$-based emissive coating was considered negligible due to its minimal thickness.
  - For sample "V", the thermal conductivity was assigned based on the typical values for polyvinyl chloride-based materials, consistent with the composition of the Vikuiti film.
- *Considered environmental parameters*
  - For validation simulations, a convective heat transfer coefficient of 2.5 W/m^{2}K was adopted, based on the operational guidelines of the climatic chamber.
  - For outdoor simulations, three standardized convective heat transfer coefficients (5 W/m^{2}K, 12 W/m^{2}K and 30 W/m^{2}K) were considered to indirectly investigate the impact of different wind speed scenarios.

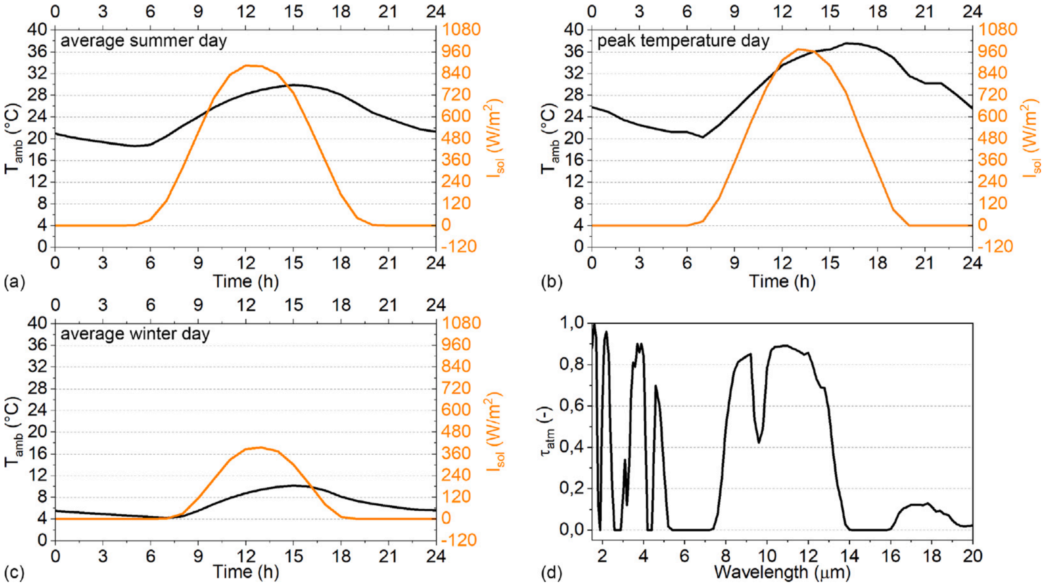

Fig. 5. Ambient temperature (T_{amb}) and solar irradiation (I_{sol}) profiles of the (a) average summer day, (b) peak temperature day of the year, and (c) average winter day, used as weather forcings to evaluate the RC performance of the investigated materials. (d) Atmospheric transmittance (τ_{atm}) profile relative to Perugia's climate.

  - Ambient temperature and solar irradiation were the only environmental forcing parameters involved for both in-chamber and outdoor analyses.

- *Modeling the radiative exchange with the atmosphere*
  - The average summer and winter days and the peak temperature day considered for outdoor simulations had clear-sky conditions: the cloudy-sky scenario was not investigated in this study.
  - Outer space temperature (T_{space}) was assumed to be equal to −270.15 °C (~ 3 K).
  - Sky temperature in clear-sky conditions (T_{sky}) was related to the ambient air temperature (T_{amb}), using a simplified empirical formulation proposed by H.P. Garg [53,54]: $T_{sky} = T_{amb} - 20$.
  - Atmospheric emittance (ε_{atm}) was implemented in COMSOL in its spectral profile, from 1.5 μm to 20 μm with a wavelength resolution of 0.2 μm. It was derived from the atmospheric transmittance profile related to Perugia's climate (τ_{atm}).
  - Atmospheric transmittance (τ_{atm}) was obtained from the predefined atmospheric profiles of the radiative transfer model SBDART (Santa Barbara DISORT Atmospheric Radiative Transfer). SBDART is a FORTRAN code designed to analyze a wide variety of radiative transfer problems encountered in satellite remote sensing and atmospheric energy budget studies [55]. Predefined atmospheric profiles are available through the parameter $idatam$, which prescribes vertical distribution of temperature, pressure, water vapor, ozone and background gases. For Perugia's atmosphere characterization, the $idatam = 6$ profile was considered (Fig. 5d), typical of a hot dry season.

To summarize, the FEM models were conceived for component-scale analyses of radiative cooling surfaces, where the main heat transfer mechanisms (solar absorption, longwave radiative exchange with the sky, and surface convection) are represented through prescribed boundary conditions rather than explicitly resolving the surrounding flow field or atmospheric dynamics. The present FEM framework was applied to three representative case-study materials and a restricted range of thermophysical properties. However, it is intrinsically capable of accommodating arbitrary combinations of thermal conductivity, density and specific heat. Wind effects were captured indirectly via convective heat transfer coefficients associated with different ventilation regimes, while atmospheric humidity was accounted for through predefined spectral transmittance profiles rather than prognostic moisture fields. The use of an empirical model for the sky temperature also introduced non-negligible limitations: even if it is a straightforward way to approximate the effective T_{sky}, it may underestimate or overestimate radiative exchange under conditions that deviate from the clear, dry reference scenario. Finally, cloud cover and its temporal variability, as well as complex three-dimensional urban geometries and interactions at building or city scale, were not explicitly resolved.

5. Results

5.1. Results from models validation

Fig. 6 compares the simulated (solid lines) and experimentally monitored (dashed lines) surface temperatures of the investigated samples under static boundary conditions inside the climatic chamber. Specifically, the surface temperature (T_{sup}), recorded during a 3-hour cycle at 30 °C and 880 W/m^2 of solar irradiation, was compared to the corresponding average surface temperature predicted by simulations. The graph focuses only on the final hour of the monitoring period, when samples were fully acclimated. Results demonstrate the good capability of the models to replicate the experimentally obtained temperatures across all samples. Indeed, the discrepancies between measured and simulated profiles fell within the experimental error margin (0.5 °C associated to the climatic chamber and 1.0 °C linked to thermocouples). Moreover, RMSE and MAE calculations demonstrated that, on average, simulated results deviated by less than 0.3 °C from experimental data (Table 2).

It is pertinent to note that, in this part of the method, T_{sup} consistently exceeded the set T_{amb} of 30 °C, regardless of the specific radiative properties of the materials. No sub-ambient cooling occurred because the samples were isolated from the actual atmospheric environment. Their heat exchange was dictated by convection and radiation processes governed by the internal conditions of the climatic chamber.

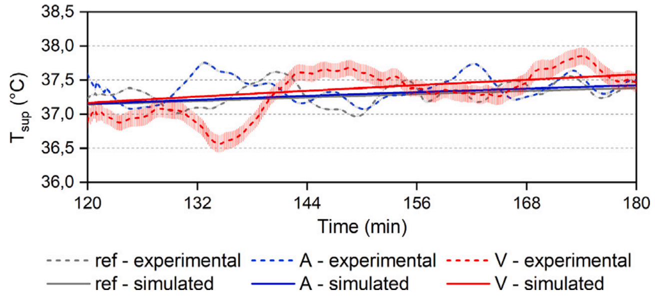

Fig. 6. Last hour of the experimental against simulated temperature monitoring of the samples under controlled environmental conditions inside the climatic chamber (T_{amb} = 30 °C, I_{sol} = 880 W/m^2).

Table 2
RMSE and MAE of the FEM models compared to the experimentally obtained T_{sup} data.

	ref	A	V
RMSE [°C]	0.17	0.20	0.28
MAE [°C]	0.14	0.15	0.22

5.2. Results from RC performance assessment

The validated FEM models were used to assess the RC performance of the investigated samples under representative outdoor conditions. The analysis focused on the temporal evolution of: (i) surface temperature of the samples relative to ambient temperature, and (ii) convective, radiative and net total heat flux exchanges between the samples and the environment, with particular emphasis on specific spectral bands relevant to radiative transfer. Results for the average summer day, warmest day of the year, and average winter day are presented in Figs. 7, 8, and 9, respectively. All scenarios were evaluated across three convective heat transfer regimes, corresponding to convection coefficients (h_c) of 5, 12 and 30 W/m^{2}K. Table 3 reports the peak superficial temperatures (T_{max}) achieved by each sample during the simulated days, alongside the corresponding convective (q_c) and radiative (q_r) fluxes entering (positive values) or leaving (negative values) the sample's surface. Fig. 10, instead, is linked to Table 3 results and shows (a) the cooling performance gains and (b) the spectral radiative gains of the investigated samples ("A" and "V") in comparison to the reference material ("ref").

5.2.1. Temperature response

The Vikuiti-based sample ("V") exhibited qualitatively distinct thermal behavior compared to the aluminum-based prototypes ("ref" and "A"), which demonstrated more similar trends reflecting their comparable material composition. All samples showed sub-ambient surface temperatures during nighttime hours, with temperature rising from the onset of solar radiation (around 6:00 for the summer-warmest scenario and 8:00 for the winter one). The non-RC reference sample ("ref") consistently attained the highest surface temperature in all conditions, establishing a performance baseline. Sample "A" showed intermediate behavior, with reduced superficial temperatures relative to "ref" due to its slightly improved emittance profile from the SiO_2-based coating. Sample "V", finally, demonstrated superior performance, maintaining sub-ambient temperatures throughout the entire 24-h simulation period.

For instance, in average summer conditions with low convection (h_c = 5 W/m^{2}K, Fig. 7a), sample "V" achieved a sub-ambient cooling of −10 °C at around 13:00, when both solar irradiation and ambient temperature were at their diurnal peaks. Under the same conditions, samples "ref" and "A" reached surface temperatures exceeding T_{amb} by 21.4 °C and 17.1 °C, respectively. These results also confirmed the poor performance of sample "A" compared to "ref": despite the material enhancement with SiO_2 particles aimed at improving its selective RC potential, no sub-ambient cooling was observed — consistent with the low spectral peak within the AW documented by the spectral characterization (Section 2.2).

This performance, hierarchy persisted during the warmest day of the year (Fig. 8a). Despite higher absolute surface temperatures due to the higher ambient temperature profile, the relative cooling magnitude remained invariant: "V" maintained −10 °C sub-ambient cooling, while "ref" and "A" reached + 23 °C and + 18 °C above ambient, respectively. Winter conditions (Fig. 9a) confirmed this consistency, underscoring the penalty incurred by non-adaptive high-emissivity materials during the cold seasons.

5.2.2. Influence of convective heat transfer

Temperature differences between ambient and samples surface systematically decreased with increasing h_c values. During daytime, elevated convective heat transfer rates cooled the aluminum-based samples ("ref" and "A") while paradoxically warming the Vikuiti-based sample ("V"), whose surface remained persistently below T_{amb}. Nocturnal convective exchange, instead, warmed all samples, approaching thermal equilibrium with the surrounding air at high h_c conditions, throughout both summer and winter cycles (Fig. 7b, 8b, 9b). This behavior reflects the fundamental mechanism governing heat exchange: when convective flux magnitude exceeds radiative flux magnitude ($|q_c| > |q_r|$), surface temperature becomes primarily dependent upon ambient air temperature and wind speed rather than material spectral properties. Peak-hour analysis (Table 3) reveals this transition explicitly: samples "ref" and "A" are dominated by radiative exchange ($|q_c| < |q_r|$) regardless of h_c value, whereas sample "V" transitions toward convection-dominated behavior ($|q_c| > |q_r|$). This distinction carries practical implications: the RC potential of "V", demonstrated at low wind speed (h_c = 5 W/m^2) diminishes under high-convection scenarios. During the warmest day of the year, at peak conditions and high convection (h_c = 30 W/m^2), sample "V" achieved only −2.7 °C sub-ambient cooling, a reduction of 74% relative to the low-convection case. Such convection-sensitivity underscores the necessity of accounting for local wind regimes in predicting the performance of RC applications.

5.2.3. Spectral analysis of radiative heat transfer

Focusing on the spectral distribution of radiative flux provides additional insights into the daytime RC potential of materials. As expected from the measured reflectance profiles (Section 2.2), all samples absorbed a portion of the incident solar radiation (0.25–2.5 μm). As highlighted in Table 3, sample "ref" and "A" concentrated absorbed solar energy within the VIS waveband (0.38–0.78 μm), whereas sample "V" exhibited almost 100% reflectivity. Similarly, "V" also showed the minimal absorption in the NIR (0.78–2.5 μm), confirming its effectiveness in rejecting solar thermal loads.

Performance differentiation intensified within the MIR spectrum (> 2.5 μm), particularly within the AW (8–13 μm). Under low convection (h_c = 5 W/m^{2}K) and peak summer conditions, sample "V" released 89.7 W/m^2 within the AW, exceeding the corresponding emission of "ref" (16.4 W/m^2) and "A" (23.0 W/m^2) by factors of 5.5 and 3.9 respectively. Such substantial radiative loss translates into measurable thermal benefits: air cooling and superficial temperature reduction.

Beyond the AW, sample "V" showed broadband emissivity across the extended MIR domain (2.5-8 μm and 13–20 μm), with out-of-window (out-AW) radiative losses of 31.6 W/m^2 under summer low wind speed, peaking at 34.6 W/m^2 during the warmest day of the year. While radiative losses outside the AW are inherently less efficient – because of the interaction with the relatively warmer atmosphere rather than the cold sink of outer space – they nonetheless contribute beneficially to the net heat rejection of a surface, as the effective sky temperature remains well below ambient air temperature.

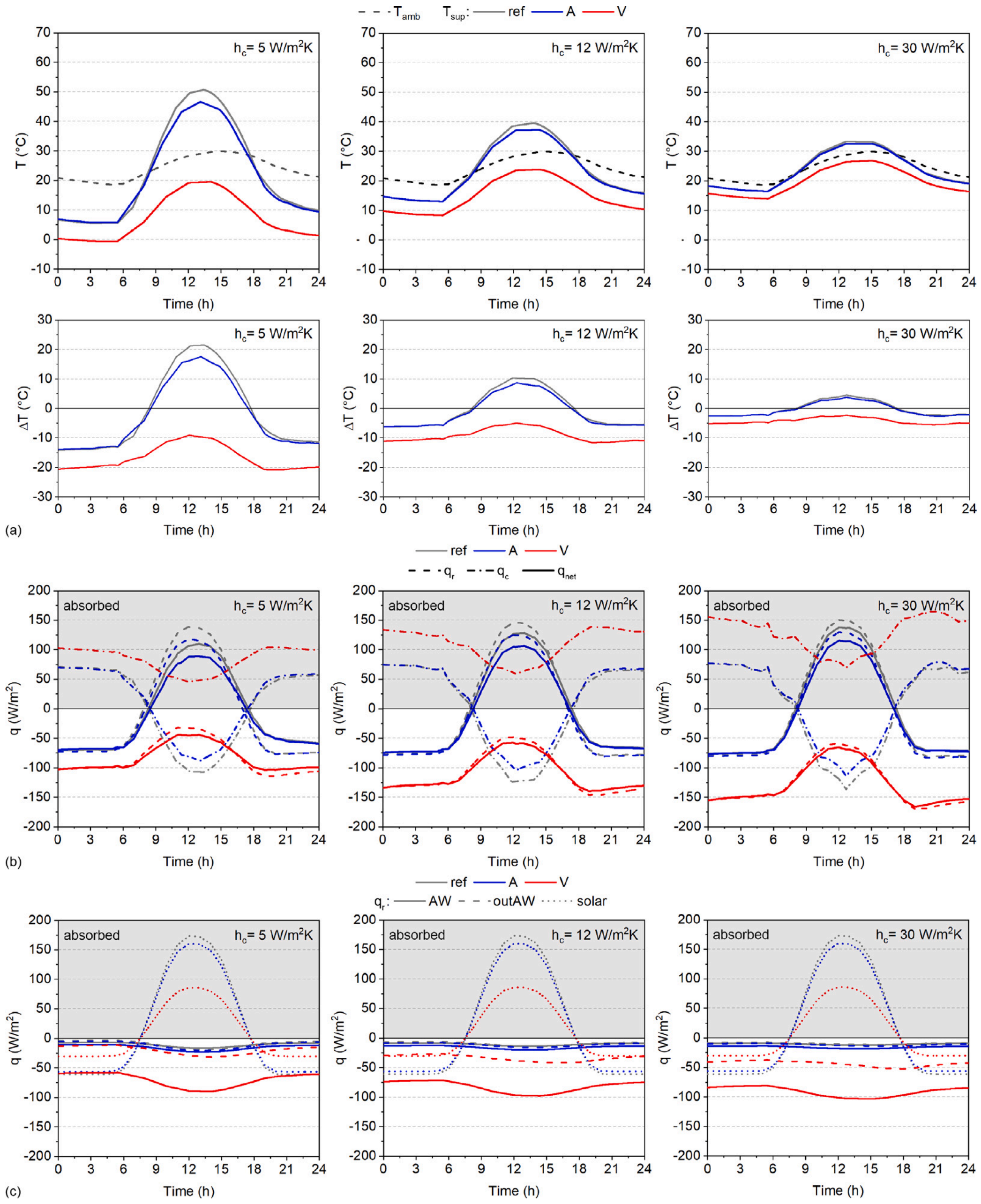

Fig. 7. Average summer day: (a) Surface temperatures (T_{sup}) of the tested samples and corresponding differences with ambient air temperature (T_{amb}). (b) Heat flux components, i.e., convective (q_c), radiative (q_r), and net total (q_{net}). (c) Spectral radiative exchanges within the solar range, the atmospheric window (AW, 8–13 μmm), and outside the AW (2.5–8 μm and 13–20 μmm). Positive fluxes (> 0; gray shaded region) denote net heat absorption by the sample. Panels are shown for low, medium, and high convection scenarios (left to right).

6. Discussion over the developed FEM models

To further evaluate the capability of the developed FEM models of accurately reproducing the RC phenomenon, additional simulations were performed using hypothetical broadband and selective emitters characterized by idealized emissivity spectra. The same numerical framework was subsequently applied to investigate the influence of atmospheric transmittance on the RC performance, by running simulations with three distinct atmospheric profiles representative of different climates and relative humidity levels.

6.1. The effect of spectral distribution on the RC performance

To isolate the effect of different spectral properties on the RC phenomenon, the here-developed FEM models were applied on idealized selective (SRC) and broadband (BRC) radiative coolers (Fig. 11). Both materials were prescribed a fixed solar reflectance at 90%, while their MIR emittance was systematically varied across three levels: low (ε =30%), medium (ε =65%) and high (ε =100%). For SRCs, emissivity outside the AW was set to 10%, optimizing the emission only within the 8–13 μm waveband. BRCs, conversely, maintained constant emittance profile across the full 2.5–20 μm spectral range. Simulations replicated

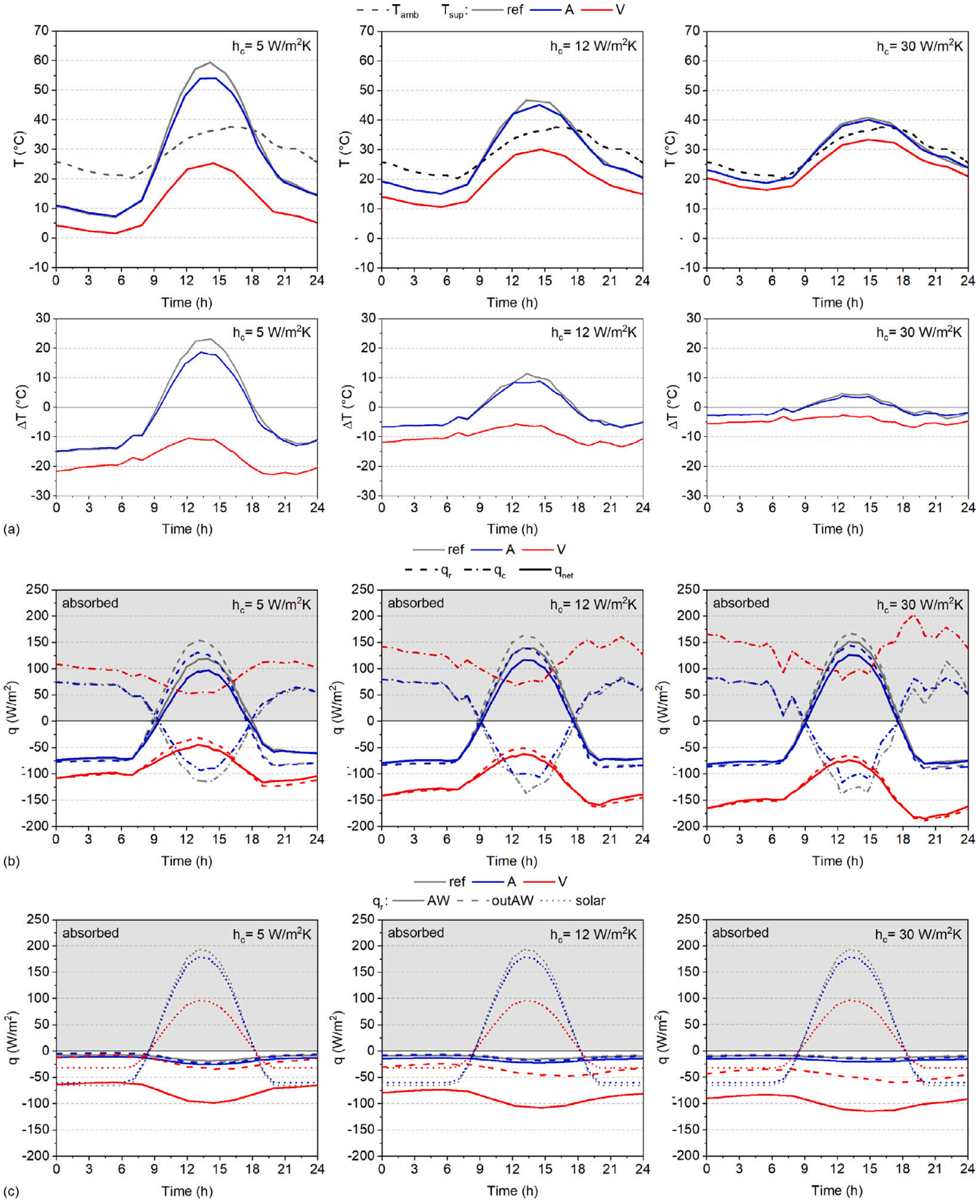

Fig. 8. Peak temperature day: (a) Surface temperatures (T_{sup}) of the tested samples and corresponding differences with ambient air temperature (T_{amb}). (b) Heat flux components, i.e., convective (q_c), radiative (q_r), and net total (q_{net}). (c) Spectral radiative exchanges within the solar range, the atmospheric window (AW, 8–13 μmm), and outside the AW (2.5–8 μm and 13–20 μmm). Positive fluxes (> 0; gray shaded region) denote net heat absorption by the sample. Panels are shown for low, medium, and high convection scenarios (left to right).

the average summer day of previous analyses under low-convection conditions (h_c=5 W/m^{2}K).

As shown Fig. 12, a pronounced dependence between material emissivity and surface temperature (T_{sup}) was demonstrated, with performance divergence between n SRC and BRC designs increasing systematically with spectral selectivity. At low emissivity (Fig. 12, top-left panel), both radiative emission and sub-ambient cooling capacity were limited, resulting in a relatively high surface temperature. However, even under these conditions, the BRC material achieved a T_{sup} approximately 3.3 °C lower than the SRC equivalent at peak solar loading, thanks to its broader radiative capacity. Such baseline advantage became more pronounced as emissivity increased: at ideal conditions of ε =100% (Fig. 12, top-right panel), BRC achieved maximum sub-ambient cooling with a temperature drop of 14.4 °C relative to T_{amb}, compared to 11.2 °C for the SRC configuration. This directly correlates with enhanced net radiative heat loss rates (negative q_r values), which were larger for BRCs through the whole simulated day. This enhancement stems from their capability of emitting not only within the AW, but also in the outer spectrum (2.5–8 μm and 13–20 μm), increasing total radiative dissipation.

The heat flux decomposition (Fig. 13) reveals the main differences in how SRCs and BRCs exploited their spectral properties to achieve RC:

- SRCs concentrated their emissive power almost exclusively within the AW waveband, with minimal contributions outside it. Under all three emissivity conditions, SRC thermal output scaled linearly with ε values, optimizing radiative loss toward the cold outer

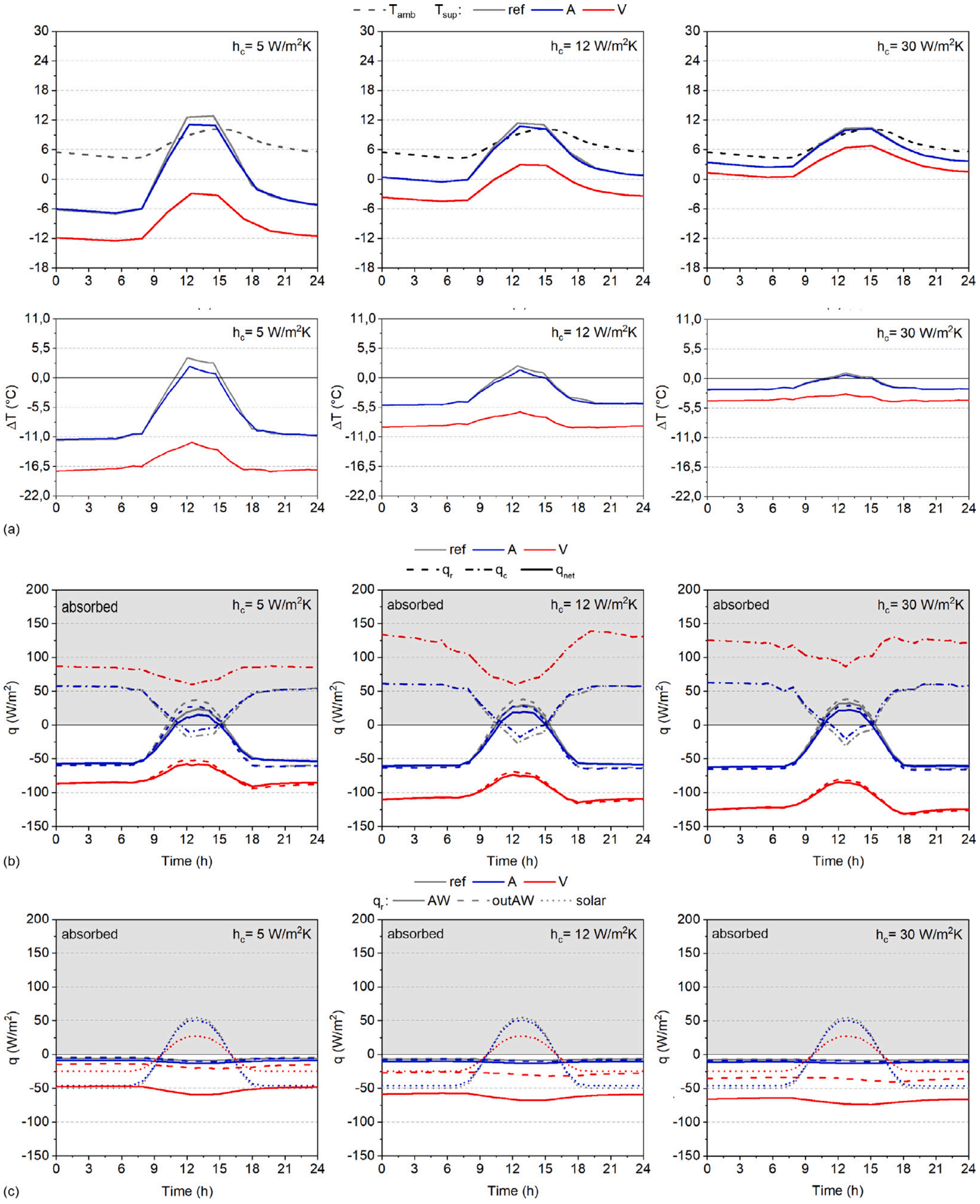

Fig. 9. Average winter day: (a) Surface temperatures (T_{sup}) of the tested samples and corresponding differences with ambient air temperature (T_{amb}). (b) Heat flux components, i.e., convective (q_c), radiative (q_r), and net total (q_{net}). (c) Spectral radiative exchanges within the solar range, the atmospheric window (AW, 8–13 μmm), and outside the AW (2.5–8 μm and 13–20 μmm). Positive fluxes (> 0; gray shaded region) denote net heat absorption by the sample. Panels are shown for low, medium, and high convection scenarios (left to right).

space and making them ideal under clear sky conditions, as marked by Raman et al. [33].

- BRCs exhibited broadband emission characteristics, with substantial out-AW band radiation. Although portions of this radiation are subject to reabsorption by atmospheric water vapor and CO_2, the energetic advantage of enhanced total radiative capacity enables BRCs to maintain effective cooling across a broader range of outdoor environmental conditions, as observed by Gentle and Smith [56].

Both SRC and BRC materials absorbed incident solar radiation across the UV/VIS/NIR range (0.25–2.5 μm), introducing a thermal load that generally scales inversely with solar reflectance properties. Under the simulated low-convection scenario, since $T_{air} > T_{sup}$ because of the enhanced radiative cooling, a convective heating mechanism occurred. Cooler surfaces draw sensible heat from the warmer surrounding air, an effect that intensified as sub-ambient cooling increased. Such phenomenon was most pronounced at high emissivity (ε = 100%), where the deepest temperature drop maximized the driving gradient for convective energy uptake. This interplay between radiative cooling and convective gain underscores the importance of modeling integrated heat transfer pathways.

6.2. The effect of atmospheric transmittance

To finally assess how atmospheric conditions modulate the RC performance, and in particular the impact of atmospheric transmittance, the FEM model for the SRC-high and BRC-high materials of Section 6.1

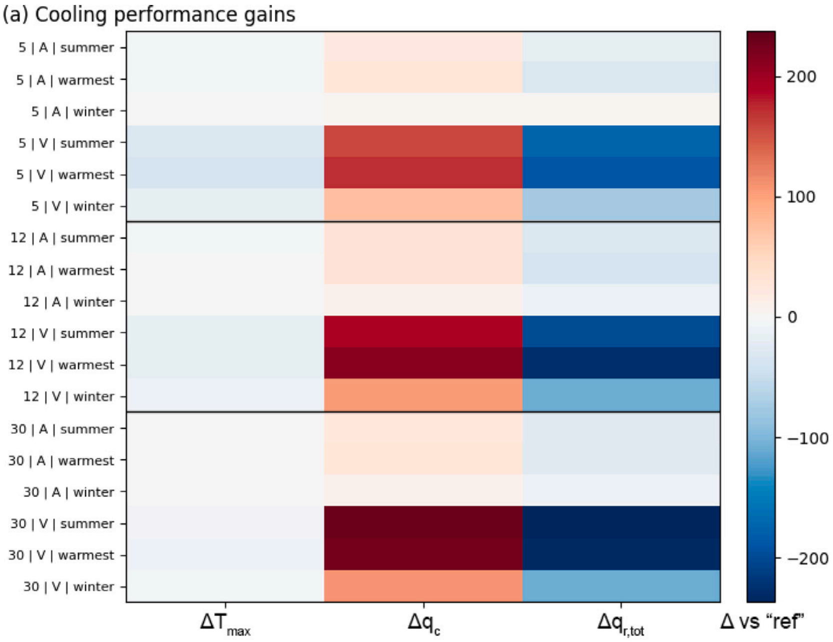

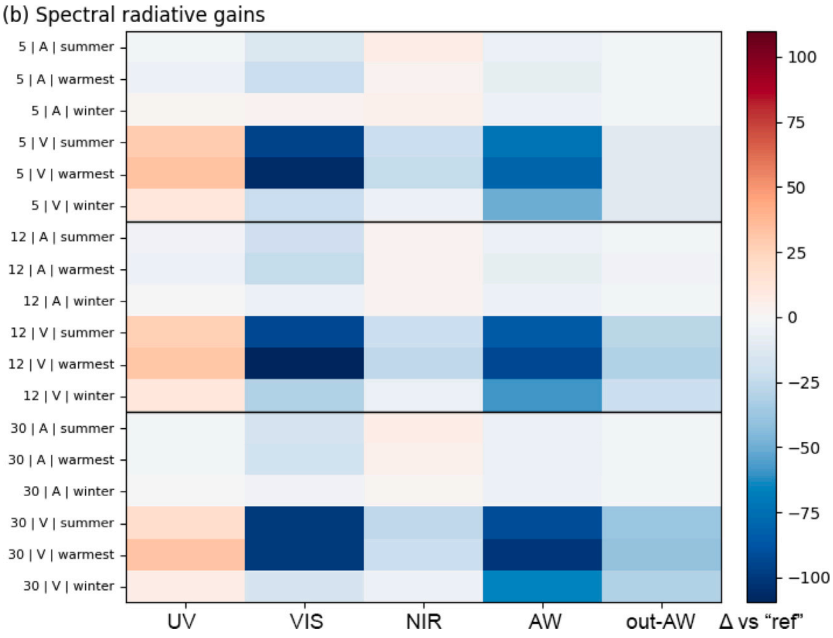

Fig. 10. Heatmaps of cooling gains relative to the "ref" sample for the "V" and "A" samples: (a) cooling performance gains and (b) spectral radiative contributions. Horizontal separators indicate different convective heat transfer coefficients. Negative values correspond to enhanced cooling performance.

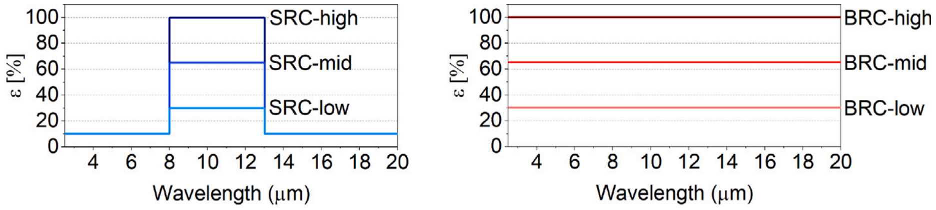

Fig. 11. Emittance profiles for the selective (SRC, on the left) and broadband (BRC, on the right) hypothetical materials considered to further test the reliability of the FEM models.

Table 3

Maximum superficial temperature (T_{max}) and corresponding convective (q_c) and radiative (q_r) fluxes exchanged between the samples and the surrounding during the simulated summer, warmest and winter days. The radiative flux q_r is resolved into distinct spectral bands: UV (0.25–0.38 μm), VIS (0.38–0.78 μm), NIR (0.78–2.5 μm), AW (8–13 μm), and out-AW (2.5–8 μm and 13–20 μm).

h_c			T_{max} [°C]	q_c [W/m^2]	q_r [W/m^2] UV	VIS	NIR	AW	out-AW	tot
5 W/m^{2}K	ref	summer	50.7	−107.4	24.1	103.15	40.4	−16.4	−19.0	132.3
		warmest	59.4	−116.2	26.8	114.8	45.0	−18.4	−21.9	146.4
		winter	12.9	−13.9	5.9	25.3	9.9	−8.8	−8.9	23.5
	A	summer	46.6	−87.9	22.6	88.9	46.6	−23.0	−21.0	114.0
		warmest	54.1	−88.9	23.3	91.8	48.1	−25.6	−23.8	113.9
		winter	11.1	−10.7	7.0	27.7	14.5	−12.8	−10.0	26.5
	V	summer	19.5	50.6	52.9	7.7	18.5	−89.7	−31.6	−42.2
		warmest	25.3	54.8	60.0	8.7	21.0	−98.6	−34.6	−43.5
		winter	−2.9	59.8	17.8	2.6	6.2	−59.2	−20.4	−52.9
12 W/m^{2}K	ref	summer	39.6	−120.7	23.3	100.0	39.2	−13.7	−13.6	135.0
		warmest	46.8	−137.6	27.6	118.2	46.3	−15.2	−15.4	161.5
		winter	11.4	−27.1	7.7	33.0	12.9	−8.6	−8.2	36.9
	A	summer	37.3	−91.0	20.0	78.7	41.2	−19.8	−16.0	104.2
		warmest	45.1	−106.4	23.8	93.5	49.0	−22.2	−18.2	125.8
		winter	10.8	−17.9	7.2	28.1	14.8	−12.7	−9.8	27.5
	V	summer	23.9	70.0	50.3	7.3	17.6	−97.8	−41.3	−63.9
		warmest	30.1	−74.9	58.7	8.5	20.5	−108.0	−45.6	65.9
		winter	2.9	75.9	18.0	2.6	6.3	−67.7	−30.0	−70.7
30 W/m^{2}K	ref	summer	33.3	−136.3	24.8	106.0	41.5	−12.3	−11.0	148.9
		warmest	40.9	−135.5	25.3	108.0	42.3	−13.8	−12.9	148.9
		winter	10.4	−7.6	4.1	17.4	6.8	−8.4	−8.2	11.7
	A	summer	32.5	−113.6	22.8	89.6	47.0	−18.2	−13.2	128.0
		warmest	40.1	−109.5	22.9	90.0	47.1	−20.4	−15.4	124.1
		winter	10.2	0.2	3.7	14.7	7.7	−12.6	−10.0	3.5
	V	summer	26.8	92.9	43.2	6.3	15.1	−103.4	−49.4	−88.1
		warmest	33.4	90.1	57.6	8.4	20.1	−114.7	−53.6	−82.1
		winter	6.8	101.5	9.3	1.4	3.2	−73.7	−38.8	−98.6

was applied to the average summer day of three representative climates. Each of them was characterized by distinct air temperature and solar irradiation profiles (T_{amb} and I_{sol}, Fig. 14a–c) and, of course, by different longwave atmospheric transmittance profiles (τ_{atm}, Fig. 14d). The selected scenarios reproduced: (i) a hot dry climate with high AW transmittance and relatively low water vapor content, (ii) a very hot humid climate, where water vapor absorption strongly attenuates the 8–13 μm window, and (iii) a cold dry climate with slightly lower ambient temperatures but enhanced longwave transparency, not only within the AW but even in the 16–20 μm range.

T_{amb} and I_{sol} profiles were derived from the PVGIS typical meteorological year generator, i.e., a tool that generates a 1-year hourly data file for a given location, according to the ISO 15927-4 procedure [57]. The average summer day was obtained by calculating the hourly mean values of T_{amb} and I_{sol} from June 1 to August 31. For τ_{atm} spectral distributions, instead, the predefined atmospheric profiles of the radiative transfer model SBDART were used, as described in Section 4.3. In this part of the study, the hot dry (*idatam* 6), very hot humid (*idatam* 1) and very cold (*idatam* 5) profiles were considered, referring to Tucson (AZ), Miami (FL) and International Falls (MN) climate, respectively (Fig. 14d).

The surface temperature (T_{sup}) evolution reported in Fig. 15a confirms that the RC effectiveness is maximized under conditions of high atmospheric transparency. In the hot dry climate, both SRC-high and BRC-high surfaces maintained T_{sup} below ambient temperature T_{amb} during the whole average summer day, with cooling reductions of ~13 °C and ~16 °C around 13:00, respectively. Conversely, in the very hot humid climate, despite a comparable T_{amb} profile, the attainable superficial temperature reduction was attenuated, with sub-ambient cooling of ~8 °C for the SRC material and ~11 °C for the BRC prototype. This behavior directly reflects the diminished MIR transmittance of the atmosphere in case of a higher content of water vapor in the air, which limits radiative heat rejection to the sky. Under the cold dry climate, SRC-high behave very similar to the hot dry scenario (~13 °C below T_{amb}, at 13:00), while BRC-high doubled the temperature distance from the selective counterpart, reaching up to −19 °C below ambient temperature. This is attributable to the higher transparency of the cold dry climate atmosphere in the 16–20 μm region, in comparison to the lower profile of the hot dry climate. That part of the spectrum, indeed, affects the radiative transfer of a broadband emitter with the sky, while does not impact the performance of a selective emitter.

Looking at Fig. 15b,c and Fig. 16 it is evident how, across all the investigated climates, the radiative term q_r generally dominates the net heat balance, confirming that atmospheric transmittance is a significant limiting factor for RC performance. In the hot dry climate, the emitted radiative flux within the AW (q_r−AW) was only partially counterbalanced by the absorbed solar radiation (q_r−UV +q_r−VIS +q_r−NIR) and convective flux (q_c), resulting in a negative net heat flux (q_{net}). In humid conditions, the reduced q_r−outAW component significantly diminished the cooling potential, even though the absorbance in the solar spectrum remained unchanged. This highlighted a crucial point: improving material spectral properties alone is insufficient when atmospheric transparency is low, as the sky effectively acts as a radiative barrier.

7. Conclusions

This study developed and validated FEM models to investigate the RC potential of three case-study materials under realistic outdoor conditions, providing new insights into their thermal behavior across different seasons, convective regimes, and spectral domains.

The models, first verified through controlled climatic chamber tests, offered a strong reliability for extrapolation to outdoor scenarios (measured-simulated temperature deviation below 0.3 °C). Results revealed marked differences in the thermal response of the investigated materials. The reference aluminum sample ("ref") consistently exhibited the highest surface temperatures, confirming its non-RC nature. The SiO_2-coated aluminum sample ("A") showed minor improvement due to its enhanced layer structure. In stark contrast,

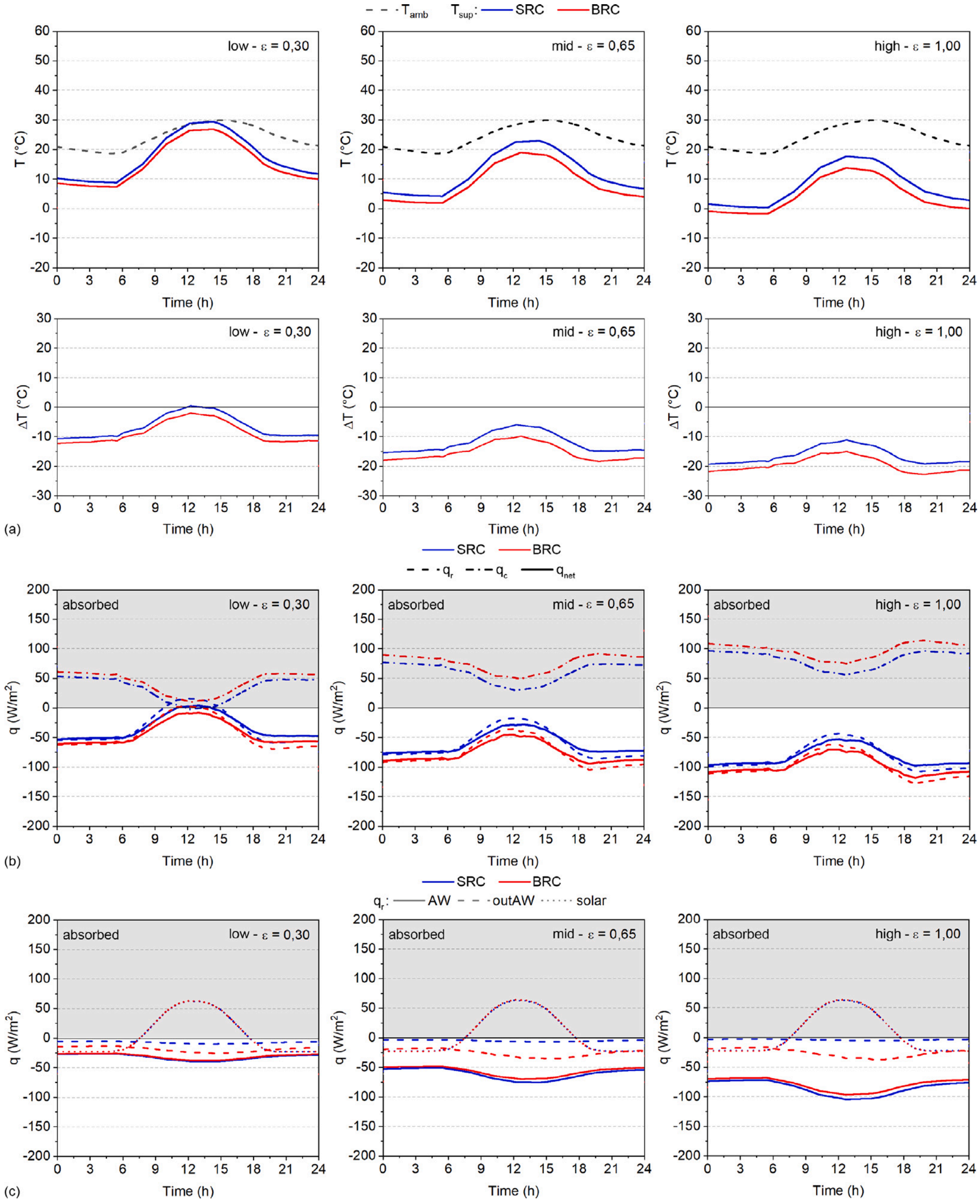

Fig. 12. Average summer day: (a) Surface temperatures (T_{sup}) of the investigated SRCs and BRCs and corresponding differences with ambient air temperature (T_{amb}). (b) Heat flux components, i.e., convective (q_c), radiative (q_r), and net total (q_{net}). (c) Spectral radiative exchanges within the solar range, the atmospheric window (AW, 8–13 μmm), and outside the AW (2.5–8 μm and 13–20 μmm). Positive fluxes (> 0; gray shaded region) denote net heat absorption by the sample. Panels are shown for low, medium, and high emissivity profiles (left to right).

the Vikuiti-based sample ("V") achieved sustained sub-ambient temperatures under summer, extremely hot, and winter conditions. In particular, the achievement of a substantial sub-ambient cooling of −10 °C during the simulated warmest day of the year, with a low convection coefficient (h_c), underscored the high potential of "V" material for passive RC applications.

The analysis of convective, radiative and net total heat fluxes indicated that while radiative processes dominated for the aluminum-based samples ("ref" and "A"), convective effects became significant for the Vikuiti-based material, especially under higher h_c values. For instance, the reduction in sub-ambient cooling for sample "V" went from −10 °C under low convection to −2 °C under high convection in peak summer conditions, emphasizing the need to consider local wind regimes when assessing the real-world effectiveness of RC materials. The spectral analysis of the radiative flux corroborated these trends, linking the enhanced cooling of "V" (over four times greater than that of "A") to high solar reflectivity and strong broadband emittance.

The here-developed FEM framework is a flexible tool capable of accommodating arbitrary combinations of materials' physical properties, together with different spectral and convective boundary conditions. It is, therefore, a promising basis for broader, systematic evaluations of RC materials across diverse design spaces and climatic contexts. In this work, the same FEM model was further applied to idealized selective (SRC) and broadband (BRC) emitters, in order to deeper investigate the impact of spectral selectivity on the overall RC performance. Under identical solar reflectance and low-convection summer conditions, a systematic divergence between SRC and BRC designs was demonstrated as emissivity increased. At ideal maximum emissivity ($\varepsilon = 100\%$),

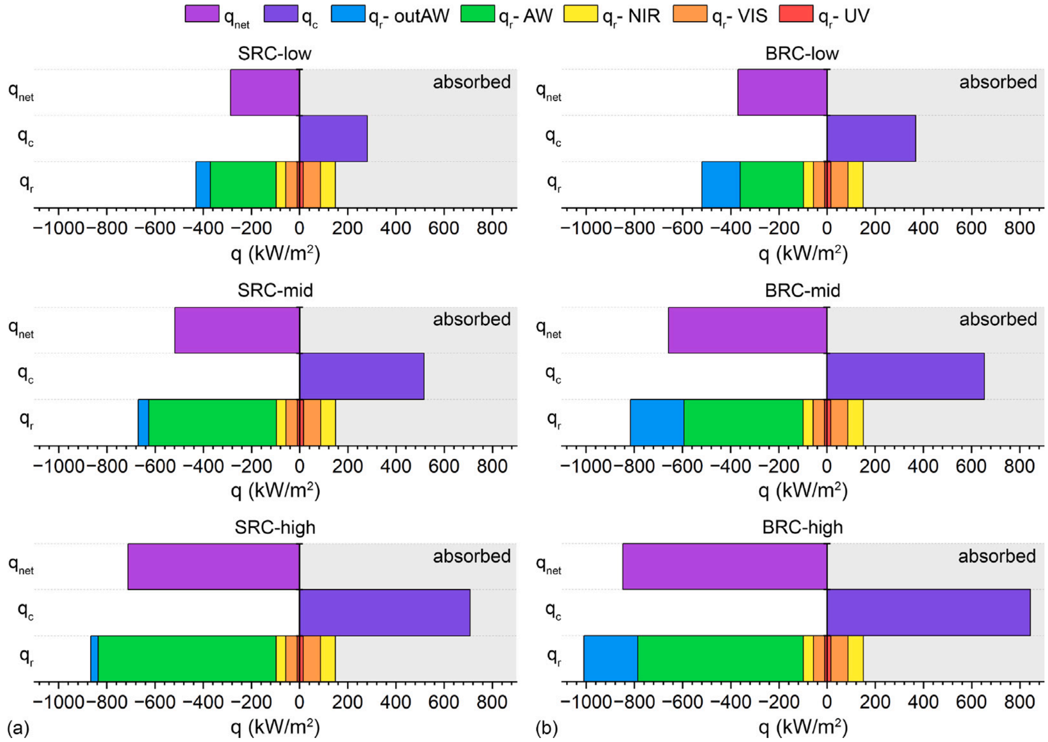

Fig. 13. Net total (q_{net}), convective (q_c) and radiative (q_r) fluxes exchanged between the investigated SRCs and BRCs and the surrounding during the simulated average summer day. The radiative flux q_r is resolved into distinct spectral bands: UV (0.25–0.38 μm), VIS (0.38–0.78 μm), NIR (0.78–2.5 μm), AW (8–13 μm), and out-AW (2.5–8 μm and 13–20 μm).

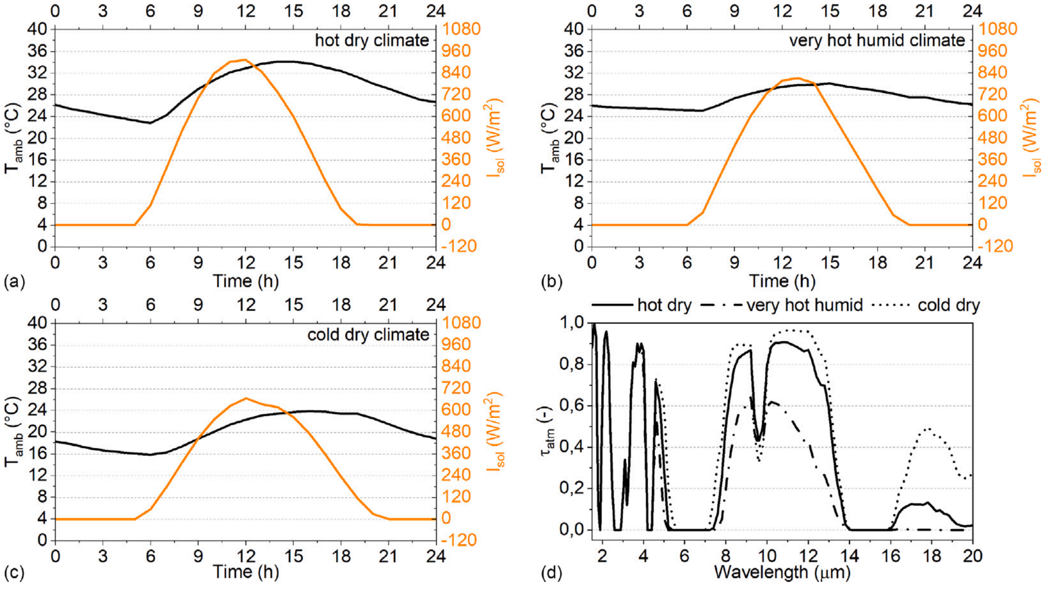

Fig. 14. Ambient temperature (T_{amb}) and solar irradiation (I_{sol}) profiles of the (a) hot dry, (b) very hot humid, and (c) cold dry climates selected to investigate the impact of different atmospheric transmittance profiles on the RC phenomenon. (d) Atmospheric transmittance (τ_{atm}) profiles relative to the three climates.

BRCs achieved a sub-ambient cooling of 14.4 °C compared to 11.2 °C for SRCs, owing to the larger net radiative loss throughout the day. Again, simulations highlighted the interplay between radiative cooling and induced convective heat gains as surface temperatures fell below ambient. Future work should focus on extending the parametric analysis to materials with markedly different thermophysical characteristics and multilayer configurations. In parallel, the current restriction to a horizontal surface under unobstructed sky should be generalized to arbitrary orientations and more complex surrounding geometries. This will include the introduction of view-factor-based descriptions of radiative exchange with neighboring structures and the assessment of tilted systems, ultimately moving the tool toward a more comprehensive support for the integration of radiative cooling materials in real building and urban environments.

Finally, by incorporating atmospheric transmittance profiles representative of different climates (hot dry, very hot humid, and cold dry), the FEM model successfully captured the modulation of RC effectiveness by humidity, water vapor content, and longwave transparency. Cooling was maximized under dry, high-transmittance conditions and attenuated in humid atmospheres. In cold dry climates,

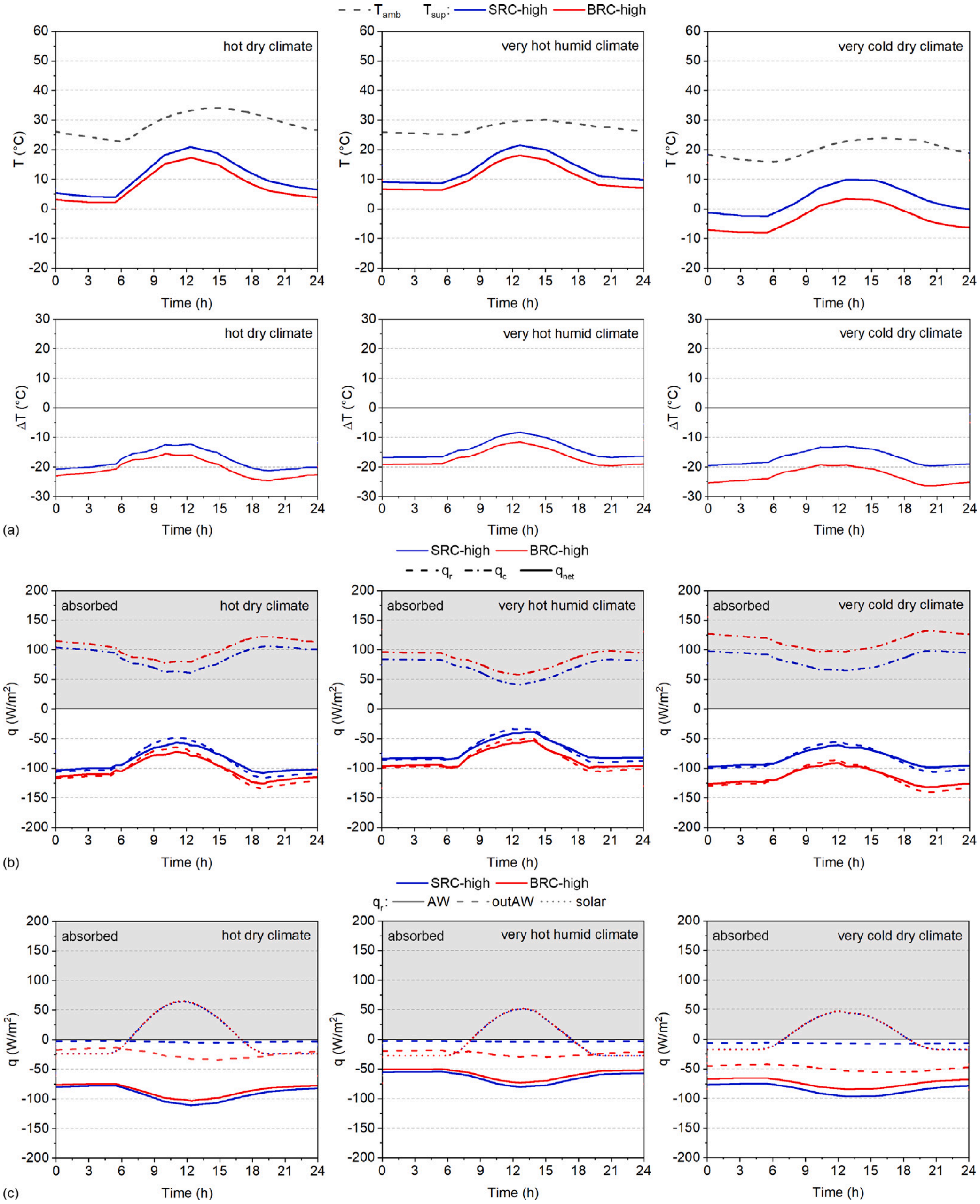

Fig. 15. Typical summer day: (a) Surface temperatures (T_{sup}) of the investigated SRC-high and BRC-high samples and corresponding differences with ambient air temperature (T_{amb}). (b) Heat flux components, i.e., convective (q_c), radiative (q_r), and net total (q_{net}). (c) Spectral radiative exchanges within the solar range, the atmospheric window (AW, 8–13 μmm), and outside the AW (2.5–8 μm and 13–20μmm). Positive fluxes (> 0; gray shaded region) denote net heat absorption by the sample. Panels are shown for hot dry, very hot humid, and very cold dry climate conditions (left to right).

broadband emitters benefited from enhanced transparency beyond the AW (16–20 μm), achieving surface temperatures up to 19 °C below ambient. In conclusion, this study demonstrates the effectiveness of validated FEM models as a powerful and flexible tool for the comprehensive analysis of radiative cooling materials. The novelty of the approach lies in its capability to investigate RC mechanisms in detail while accounting for different atmospheric conditions and materials' properties, without resorting to computationally intensive radiative transfer solvers.

On the other hand, while the modeling results highlight the strong theoretical potential of RC materials under favorable atmospheric and convective conditions, they should not be interpreted as a direct indication of immediate large-scale applicability. Practical deployment in the built environment requires careful consideration of additional factors, including long term durability of optical properties, material aging and soiling, different environmental boundary conditions (e.g., cloudy sky), economic viability, and compatibility with conventional construction systems and building envelopes. The FEM framework presented here is intended as a predictive and comparative tool to support material design and climate-specific optimization, rather than as a substitute for full-scale experimental validation and techno-economic assessment. Future work should therefore couple the proposed modeling approach with durability testing, building-scale integration studies and more advanced atmospheric and/or meteorological datasets to more comprehensively assess the real-world feasibility of radiative cooling technologies.

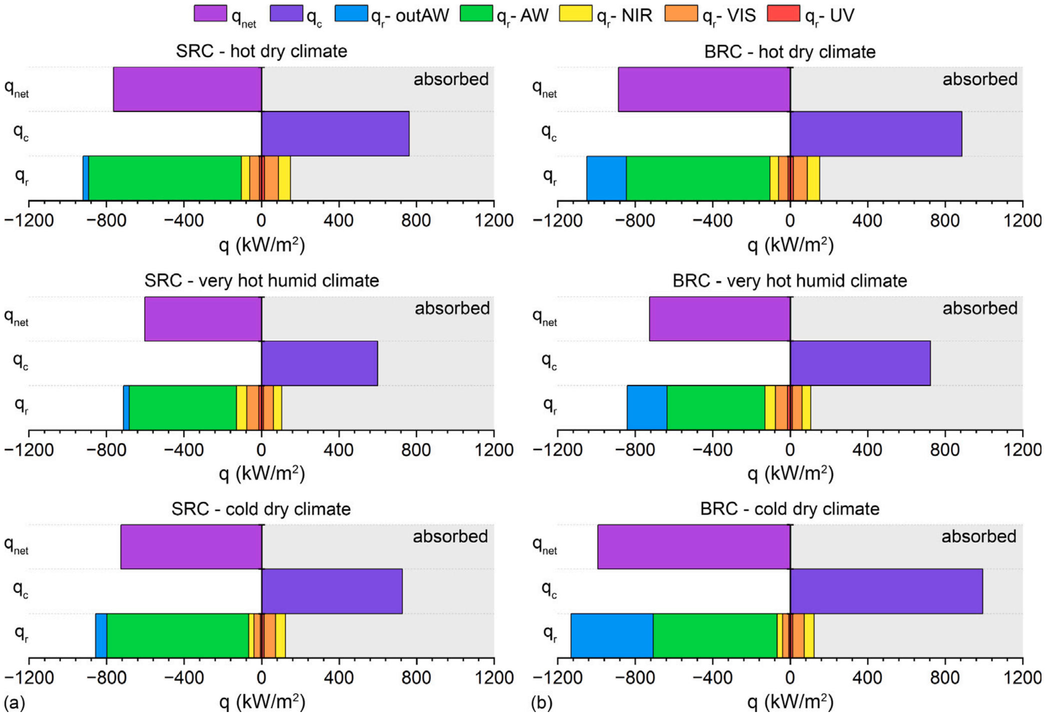

Fig. 16. Net total (q_{net}), convective (q_c) and radiative (q_r) fluxes exchanged between the investigated SRC-high and BRC-high and the surrounding during the simulated typical day of hot dry, very hot humid and cold dry climate. The radiative flux q_r is resolved into distinct spectral bands: UV (0.25–0.38 μm), VIS (0.38–0.78 μm), NIR (0.78–2.5 μm), AW (8–13 μm), and out-AW (2.5–8 μm and 13–20 μm).

CRediT authorship contribution statement

Chiara Chiatti: Writing – original draft, Visualization, Validation, Software, Methodology, Investigation, Formal analysis, Data curation, Conceptualization. **Claudia Fabiani:** Writing – review & editing, Visualization, Supervision, Investigation, Methodology, Conceptualization. **Anna Laura Pisello:** Writing – review & editing, Supervision, Investigation, Resources, Project administration, Funding acquisition, Conceptualization.

Declaration of Generative AI and AI-assisted technologies in the writing process

During the preparation of this work the authors used ChatGPT in order to improve the English of some parts of the text. After using this service, the authors reviewed and edited the content as needed and take full responsibility for the content of the published article.

Declaration of competing interest

The authors declare that they have no known competing financial interests or personal relationships that could have appeared to influence the work reported in this paper.

Acknowledgments

Funded by the European Research Council within the framework of Horizon Europe Programme (ERC-StG-2021, HELIOS, G.A. 101041255 and ERC-PoC-2024, FOR REAL, G.A. 101213070). Views and opinions expressed are, however, those of the authors only and do not necessarily reflect those of the European Union or the European Research Council. Neither the European Union nor the granting authority can be held responsible for them. All authors revised and gave approval to the final version of the manuscript.

Data availability

Data will be made available on request.

References

[1] Solecki W, Roberts D, Seto KC. Strategies to improve the impact of the IPCC special report on climate change and cities. Nat Clim Chang 2024;14:685–91. http://dx.doi.org/10.1038/s41558-024-02060-9.

[2] Ren Y, Lafortezza R, Giannico V, Sanesi G, Zhang X, Xu C. The unrelenting global expansion of the urban heat island over the last century. Sci Total Environ 2023;880. http://dx.doi.org/10.1016/j.scitotenv.2023.163276.

[3] Liu S, Cai M, Ren C, Chen G, Nielsen CP, Samuelson H. Urban heat island impacts on cooling energy demand of residential buildings at the city scale: a case study of Hong Kong. Energy 2025;332. http://dx.doi.org/10.1016/j.energy.2025.137165.

[4] Jabbar H, Hamoodi M, Al-Hameedawi A. Urban heat islands: a review of contributing factors, effects and data. IOP Conf Ser: Earth Environ Sci 2023;1129:012038. http://dx.doi.org/10.1088/1755-1315/1129/1/012038.

[5] Chen J, Wang H, Zhu H. Analytical approach for evaluating temperature field of thermal modified asphalt pavement and urban heat island effect. Appl Therm Eng 2017;113:739–48. http://dx.doi.org/10.1016/j.applthermaleng.2016.11.080.

[6] Yu X, Chan J, Chen C. Review of radiative cooling materials: Performance evaluation and design approaches. Nano Energy 2021;88:106259. http://dx.doi.org/10.1016/j.nanoen.2021.106259.

[7] Kim D-H, Park K, Baik J-J, Jin H-G, Han B-S. Contrasting interactions of urban heat islands with dry and moist heat waves and their implications for urban heat stress. Urban Clim 2024;56:102050. http://dx.doi.org/10.1016/j.uclim.2024.102050.

[8] Chiatti C, Fabiani C, Cotana F, Pisello AL. Exploring the potential of photoluminescence for urban passive cooling and lighting applications: A new approach towards materials' optimization. Energy 2021. http://dx.doi.org/10.1016/j.energy.2021.120815.

[9] Xuan Q, Lei L, Wang T, Jiang B, Zhao B, Li G, Peo G, Dai J-GD. New insights into building-integrated radiative cooling for near-ambient temperature regulation. Energy 2025;335. http://dx.doi.org/10.1016/j.energy.2025.138008.

[10] Li Z, Chen J, Wang C, Wang W, Fu Y, Chen X, Zhang R, Pan A, Ho TC, Lin K, Liang L, Tso CY. Enhancing sustainable urban environments in China: Daytime radiative cooling for building energy efficiency and heat island mitigation. Appl Energy 2025;393. http://dx.doi.org/10.1016/j.apenergy.2025.126138.

[11] Pandiyan R, Praveen Kumar G. Experimental analysis of a sky radiative cooling system and numerical investigation of its integration with a chiller and energy storage system for sustainable cooling applications. Appl Therm Eng 2025;275. http://dx.doi.org/10.1016/j.applthermaleng.2025.126813.

[12] Chen H, Wei J, Liu X, Liu J, Wang C. Assessing radiative cooling power considering the cloud effects. Appl Therm Eng 2025;278. http://dx.doi.org/10.1016/j.applthermaleng.2025.127192.

[13] Zhang W, Pei G, Zhao B. Performance analysis of switchable radiative cooling and solar heating for building energy-saving. Energy 2025;333. http://dx.doi.org/10.1016/j.energy.2025.137507.

[14] Bartoli B, Catalanotti S, Coluzzi B, Cuomo V, Silvestrini V, Troise G. Nocturnal and diurnal performances of selective radiators. Appl Energy 1977;3(4):267–86. http://dx.doi.org/10.1016/0306-2619(77)90015-0.

[15] Hassanien RHE, Zhao B, Hadibi T, Pei G. Progress of radiative cooling films and nanofluids in greenhouses for energy and water-saving. Appl Therm Eng 2025;279. http://dx.doi.org/10.1016/j.applthermaleng.2025.127493.

[16] Yu J, Park C, Kim B, Sung S, Kim H, Lee J, Kim YS, Yoo Y. Enhancing passive radiative cooling films with hollow yttrium-oxide spheres insights from FDTD simulation. Macromol Rapid Commun 2025;46. http://dx.doi.org/10.1002/marc.202400770.

[17] Cui C, Lu J, Zhang S, Su J, Han J. Hierarchical-porous coating coupled with textile for passive daytime radiative cooling and self-cleaning. Sol Energy Mater Sol Cells 2022;247. http://dx.doi.org/10.1016/j.solmat.2022.111954.

[18] Chiara C, Ioannis K, Fabiani C, Anna Laura P. Effect of optimized photoluminescence on luminous and passive cooling potential: A new combined experimental and numerical approach applied to yellow-emitting glass tiles. Renewable Energy 2022;196:28–39. http://dx.doi.org/10.1016/j.renene.2022.06.027.

[19] Synnefa A, Santamouris M, Livada I. A study of the thermal performance of reflective coatings for the urban environment. Sol Energy 2006;80:968–81. http://dx.doi.org/10.1016/j.solener.2005.08.005.

[20] Costanzo V, Evola G, Marletta L. Cool roofs for passive cooling: performance in different climates and for different insulation levels in Italy. Adv Build Energy Res 2013;7:155–69. http://dx.doi.org/10.1080/17512549.2013.865556.

[21] Yu J, Park C, Kwon D, Choi M, Lee J, Yoo Y. Colored and paintable polyurethane dispersion coatings for sustainable building applications. Energy 2025;330. http://dx.doi.org/10.1016/j.energy.2025.136840.

[22] Ferrari C, Muscio A, Siligardi C, Manfredini T. Design of a cool color glaze for solar reflective tile application. Ceram Int 2015;41:11106–16. http://dx.doi.org/10.1016/j.ceramint.2015.05.058.

[23] Park C, Park C, Park S, Lee J, Kim YS, Yoo Y. Hybrid emitters with raspberry-like hollow SiO2 spheres for passive daytime radiative cooling. Chem Eng J 2023;459. http://dx.doi.org/10.1016/j.cej.2023.141652.

[24] Bu F, Yan D, Tan G, Sun H, An J. Systematically incorporating spectrum-selective radiative cooling into building performance simulation: Numerical integration method and experimental validation. Appl Energy 2022;312. http://dx.doi.org/10.1016/j.apenergy.2022.118733.

[25] Zhao B, Hu M, Ao X, Chen N, Pei G. Radiative cooling: A review of fundamentals, materials, applications, and prospects. Appl Energy 2019;236:489–513. http://dx.doi.org/10.1016/j.apenergy.2018.12.018.

[26] Lee J, Im D, Sung S, Yu J, Kim H, Lee J, Yoo Y. Scalable and efficient radiative cooling coatings using uniform-hollow silica spheres. Appl Therm Eng 2024;254. http://dx.doi.org/10.1016/j.applthermaleng.2024.123810.

[27] Mandal J, Yang Y, Yu N, Raman AP. Paints as a scalable and effective radiative cooling technology for buildings. Joule 2020;4:1350–6. http://dx.doi.org/10.1016/j.joule.2020.04.010.

[28] Liang L, Bai S, Lin K, Kwok CT, Chen S, Zhu Y, Tso CY. Advancing sustainable development: Broad applications of passive radiative cooling. Sustainability 2024;16:2346. http://dx.doi.org/10.3390/su16062346.

[29] Khan A, Carlosena L, Feng J, Khorat S, Khatun R, Doan Q-V, Santamouris M. Optically modulated passive broadband daytime radiative cooling materials can cool cities in summer and heat cities in winter. Sustainability 2022;14:1110. http://dx.doi.org/10.3390/su14031110.

[30] He Y, Lu B, Fang J, Lei Y, Gao S, Feng C. Radiative cooling for long-term building energy efficiency: an experimental comparison of seven coatings. Natl Sci Open 2024. http://dx.doi.org/10.1360/nso/20230065.

[31] Huang K, Huang Z, Du Y, Liang Y, Liu J, Yan J. Advances in radiative cooling materials for building energy efficiency: a decade of progress. J Mater Chem A 2024;12:28682–710. http://dx.doi.org/10.1039/D4TA04942J.

[32] Di Han, Ng BF, Wan MP. Preliminary study of passive radiative cooling under Singapore's tropical climate. Sol Energy Mater Sol Cells 2020;206:110270. http://dx.doi.org/10.1016/j.solmat.2019.110270.

[33] Raman AP, Anoma MA, Zhu L, Rephaeli E, Fan S. Passive radiative cooling below ambient air temperature under direct sunlight. Nature 2014;515:540–4. http://dx.doi.org/10.1038/nature13883.

[34] Tso CY, Chan KC, Chao CYH. A field investigation of passive radiative cooling under Hong Kong's climate. Renew Energy 2017;106:52–61. http://dx.doi.org/10.1016/j.renene.2017.01.018.

[35] Bao H, Yan C, Wang B, Fang X, Zhao CY, Ruan X. Double-layer nanoparticle-based coatings for efficient terrestrial radiative cooling. Sol Energy Mater Sol Cells 2017;168:78–84. http://dx.doi.org/10.1016/j.solmat.2017.04.020.

[36] Yin X, Yang R, Tan G, Fan S. Terrestrial radiative cooling: Using the cold universe as a renewable and sustainable energy source. Science 2020;370:786–91. http://dx.doi.org/10.1126/science.abb0971.

[37] Zhou L, Yin X, Gan Q. Best practices for radiative cooling. Nat Sustain 2023;6:1030–2. http://dx.doi.org/10.1038/s41893-023-01170-0.

[38] Akbari H, Levinson R, Berdahl P. ASTM standards for measuring solar reflectance and infrared emittance of construction materials and comparing their steady-state surface temperatures. 1996, URL https://api.semanticscholar.org/CorpusID:36441738.

[39] Claudia F, Alberto M, Anna Laura P. Introducing the enhanced solar reflectance index (sri*) for comprehensive evaluation of spectrally selective cool materials in real-world scenarios. Sustain Energy Technol Assess. 2025;81. http://dx.doi.org/10.1016/j.seta.2025.104415.

[40] Chiatti C, Marchini F, Fabiani C, Kousis I, Carlosena L, Pisello AL. Harnessing the potential of radiative cooling for the built environment: a cutting-edge protocol for materials' characterization. Sol Energy Mater Sol Cells 2024.

[41] Piselli C, Castaldo VL, Pisello AL. How to enhance thermal energy storage effect of PCM in roofs with varying solar reflectance: Experimental and numerical assessment of a new roof system for passive cooling in different climate conditions. Sol Energy 2019;192:106–19. http://dx.doi.org/10.1016/j.solener.2018.06.047.

[42] Fabiani C, Gambucci M, Chiatti C, Zampini G, Latterini L, Pisello AL. Towards field implementation of photoluminescence in the built environment for passive cooling and lighting energy efficiency. Appl Energy 2022;324:119687. http://dx.doi.org/10.1016/j.apenergy.2022.119687.

[43] Vedrtnam A, Chaturvedi S, Gunwant D, Soares N, Ostertag CP, Kalauni K, Palou M, Cekon M, Taylor HK. Combined CFD and FEM analysis of 3D printed PCM integrated concrete panels for passive thermal management in buildings. Appl Therm Eng 2025;279. http://dx.doi.org/10.1016/j.applthermaleng.2025.127544.

[44] Liu D, He W, Wei L, Guo H. Enhanced radiative cooling of columnar thermal barrier coatings at ultrahigh temperatures and mechanisms underneath. J Mater Sci Technol 2025;239:81–92. http://dx.doi.org/10.1016/j.jmst.2025.02.073.

[45] Tahir R, Bingbing Z. Virtual prototyping approach for package delamination risk assessment under simulated high temperature exposure using finite element analysis. 2022-October, 2022, http://dx.doi.org/10.1109/IEMT55343.2022.9969510,

[46] Carlosena L, Andueza A, Torres L, Irulegi O, Hernàndez-Minguillon RJ, Sevilla J, Santamouris M. Experimental development and testing of low-cost scalable radiative cooling materials for building applications. Sol Energy Mater Sol Cells 2021;230:111209. http://dx.doi.org/10.1016/j.solmat.2021.111209.

[47] Balocco C, Petrone G. Numerical modelling for the thermal performance assessment of a semi-opaque façade with a multilayer of nano-structured and phase change materials. Buildings 2017;7(4). http://dx.doi.org/10.3390/buildings7040090.

[48] de Bona F, Benasciutti D, Moro L, Srnec Novak J. Material modelling in multiphysics FEM simulation. Key Eng Mater 2018;783:41–5. http://dx.doi.org/10.4028/www.scientific.net/KEM.783.41.

[49] Xu X, Wang N, Li X, Yang L, Wang F. A novel carbonated inorganic radiative cooling material and its spectral manipulation mechanism. Chem Eng J 2025;517. http://dx.doi.org/10.1016/j.cej.2025.164444.

[50] Gentle AR, Smith GB. A subambient open roof surface under the mid-summer sun. Adv Sci 2015;2. http://dx.doi.org/10.1002/advs.201500119.

[51] Fabian M, Lewis E, Newe T, Lochmann S. Optical fibre cavity for ring-down experiments with low coupling losses. Meas Sci Technol 2010;21:094034. http://dx.doi.org/10.1088/0957-0233/21/9/094034.

[52] ASTM International. E1980-11: Standard practice for calculating solar refectance index of horizontal and low sloped opaque surfaces. 2019, http://dx.doi.org/10.1520/E1980-11R19.

[53] Garg HP, Bannerot RB. Treatise on solar energy, volume I: Fundamentals of solar energy. J Sol Energy Eng 1983;105(4):469. http://dx.doi.org/10.1115/1.3266415.

[54] Evangelisti L, Guattari C, Asdrubali F. On the sky temperature models and their influence on buildings energy performance: A critical review. Energy Build 2019;183:607–25. http://dx.doi.org/10.1016/j.enbuild.2018.11.037.

[55] José Marcelo LJ, Juan Carlos C, Simone Marilene SdC, Francisco Luiz Ld, Hollan Sd, André RG. A physical parameterization for cloudy-sky downward longwave radiation: Validation for tropical and subtropical regions in Brazil. J Atmos Sol-Terr Phys 2025;271. http://dx.doi.org/10.1016/j.jastp.2025.106512.

[56] Gentle A, Smith G. Radiative heat pumping from the earth using surface phonon resonant nanoparticles. Nano Lett 2010;10(2):373–9. http://dx.doi.org/10.1021/nl903271d.

[57] Thomas H, Elena P, Paolo Z, Irene PP. Assembling typical meteorological year data sets for building energy performance using reanalysis and satellite-based data. Atmosphere 2018;9. http://dx.doi.org/10.3390/atmos9020053.